

## RESEARCH ARTICLE

## Characterizing convective cold pools

10.1002/2016MS000788

Aryeh J. Drager<sup>1</sup>  and Susan C. van den Heever<sup>1</sup> 

<sup>1</sup>Department of Atmospheric Science, Colorado State University, Fort Collins, Colorado, USA

### Key Points:

- A new cold pool identification and tracking algorithm for numerical model outputs is introduced
- The algorithm successfully identifies convective cold pool boundaries, including colliding convective cold pools
- Cold pool dissipation is delayed in “wet patch” regions near cold pool center where the ground has been previously soaked by precipitation

### Correspondence to:

A. J. Drager,  
Aryeh.Drager@colostate.edu

### Citation:

Drager, A. J., and S. C. van den Heever (2017), Characterizing convective cold pools, *J. Adv. Model. Earth Syst.*, 9, 1091–1115, doi:10.1002/2016MS000788.

Received 25 AUG 2016

Accepted 24 MAR 2017

Accepted article online 28 MAR 2017

Published online 9 MAY 2017

**Abstract** Cold pools produced by convective storms play an important role in Earth’s climate system. However, a common framework does not exist for objectively identifying convective cold pools in observations and models. The present study investigates convective cold pools within a simulation of tropical continental convection that uses a cloud-resolving model with a coupled land-surface model. Multiple variables are assessed for their potential in identifying convective cold pool boundaries, and a novel technique is developed and tested for identifying and tracking cold pools in numerical model simulations. This algorithm is based on surface rainfall rates and radial gradients in the density potential temperature field. The algorithm successfully identifies near-surface cold pool boundaries and is able to distinguish between connected cold pools. Once cold pools have been identified and tracked, composites of cold pool evolution are then constructed, and average cold pool properties are investigated. Wet patches are found to develop within the centers of cold pools where the ground has been soaked with rainwater. These wet patches help to maintain cool surface temperatures and reduce cold pool dissipation, which has implications for the development of subsequent convection.

## 1. Introduction

A convective cold pool is a region of evaporatively cooled air that has been transported to the surface through convective downdrafts and has then, upon reaching the surface, spread out as a density current [Simpson, 1969; Charba, 1974]. As cold pools expand, they displace warmer ambient air [Goff, 1976]. This more buoyant environmental air is then uplifted, and new clouds can form as a result [Goff, 1976; Warner *et al.*, 1980]. Colliding cold pools can be a particularly effective trigger for new convection [Droegemeier and Wilhelmson, 1985]. Furthermore, cold pools bring gusty winds that enhance sensible and latent heat fluxes, which in turn modify the thermodynamic properties and moisture structure of the subcloud layer [Tompkins, 2001; Langhans and Romps, 2015]. Convective cold pools therefore play an important role in multiple aspects of Earth’s climate system, including the maintenance of long-lived squall lines [Rotunno *et al.*, 1988; Weisman and Rotunno, 2004], the self-aggregation of tropical convection [Jeevanjee and Romps, 2013], and the shallow-to-deep transition of tropical convection [Khairoutdinov and Randall, 2006].

Limited understanding exists of the processes that determine the evolution of cold pool properties, such as cold pool strength, cold pool size, and cold pool lifetime. Work by Grant and van den Heever [2015] has shown that environmental factors such as dry layers and aerosol loading can impact cold pool vigor, and recent work by Gentine *et al.* [2016] and Grant and van den Heever [2016] has emphasized the importance of surface fluxes and entrainment of environmental air for cold pool size and longevity. By investigating how various factors affect cold pool properties, we can improve our understanding of how the role of cold pools will change under different environmental conditions.

In numerical models, one approach for investigating convective cold pools is to track individual cold pools over their respective lifetimes. Such an approach allows composites to be constructed from collections of cold pools and also permits statistics to be calculated regarding various cold pool attributes. However, cold pool tracking is not a straightforward task, even in numerical simulations where all state variables, forcing terms, and time tendencies are known quantities. Cold pool boundaries often intersect, and new cold pools frequently form on the periphery of preexisting cold pools [Tompkins, 2001; Feng *et al.*, 2015].

Several methods have emerged for identifying and characterizing convective cold pools. One method, used by Tompkins [2001], is to define cold pool air according to a buoyancy threshold, where buoyancy is defined, following Tompkins [2001] and Emanuel [1994], as

© 2017. The Authors.

This is an open access article under the terms of the Creative Commons Attribution-NonCommercial-NoDerivs License, which permits use and distribution in any medium, provided the original work is properly cited, the use is non-commercial and no modifications or adaptations are made.

$$B = g \frac{\theta_\rho - \bar{\theta}_\rho}{\bar{\theta}_\rho}, \quad (1)$$

where  $g$  is the acceleration due to gravity and  $\theta_\rho$  is the density potential temperature, defined as

$$\theta_\rho = \theta \frac{1 + \frac{R_v}{R_d} r_v}{1 + r_v + r_{cond}} \approx \theta (1 + 0.608 r_v - r_{cond}), \quad (2)$$

where  $\theta$  is the potential temperature,  $r_v$  is the mass mixing ratio of water vapor,  $r_{cond}$  is the mass mixing ratio of condensate, and  $R_v$  and  $R_d$  are the gas constants of water vapor and dry air, respectively. The overbar in  $\bar{\theta}_\rho$  in (1) denotes an “environmental” or reference value of density potential temperature, often obtained from some horizontal average or taken to be the model base state value. All locations with buoyancy below the threshold are considered to be part of a cold pool; *Tompkins* [2001], for example, uses a threshold of  $-0.005 \text{ m s}^{-2}$ . One limitation of this method of defining cold pool air is that buoyancy is defined as a relative quantity. That is, a parcel’s buoyancy is determined by whether it is more or less dense than the “environmental” or reference value. However, as *Doswell and Markowski* [2004] explain, buoyancy (in a conceptual sense) is fundamentally not a relative quantity, and the choice of an “environmental” or reference value is arbitrary. A buoyancy threshold used in one study may not be appropriate for use in a different study, and the results may not be directly comparable.

Another limitation of this method is that a buoyancy threshold alone is insufficient for identifying discrete cold pool objects. Colliding cold pools or cold pools forming on the edges of existing cold pools may be connected to each other when the buoyancy threshold is applied. *Tompkins* [2001] sidesteps this issue by identifying individual cold pools manually. Manual identification, however, contains some element of subjectivity and is impractical in cases where more than a few dozen cold pools must be identified. *Feng et al.* [2015] uses an objective, automated approach to identifying individual cold pools. In this approach, cold pool air is defined according to a buoyancy threshold of  $-0.003 \text{ m s}^{-2}$ , and contiguous regions of cold pool air are then partitioned using a watershed technique. This technique allows connected cold pools to be distinguished from one another. However, it yields cold pool boundaries that in many cases manifest as straight lines [*Feng et al.*, 2015, Figure 4c], rather than the more circular forms that are more typical of tropical convective cold pools [*Tompkins*, 2001].

*Torri et al.* [2015] and *Torri and Kuang* [2016a] have introduced a Lagrangian approach to cold pool tracking that tracks individual cold pool “particles” and designates the model grid boxes containing them as cold pool grid boxes. Regions of connected cold pool grid boxes are then designated as cold pools. Although this method is innovative in its use of a Lagrangian approach, it relies on simple  $\theta_\rho$  thresholding (cold pool particles are defined as having  $\theta_\rho$  at least 1 K below the horizontal mean) and does not make any effort to distinguish between cold pools that are connected.

Another automated approach, developed by *Gentine et al.* [2016], is to apply a k-means image segmentation algorithm to the virtual temperature ( $T_v$ ) field. In this approach, each pixel is categorized as cold pool air or non-cold-pool air. This approach does not, however, distinguish between connected cold pools, resulting in overestimation of individual cold pool areas. Furthermore, the resulting cold pools do not have clean boundaries in that isolated pixels within cold pools may be categorized as non-cold-pool air, and vice versa [*Gentine et al.*, 2016, Figure 1].

The primary goal of the present work is to develop a new automated cold pool identification and tracking algorithm for numerical model outputs that avoids the limitations of existing methods. Once this algorithm has been developed, it can be used to study populations of cold pools. The structure of the remainder of this paper is as follows: section 2 introduces the setup of the numerical model simulation that is used to develop the cold pool identification and tracking algorithm. Then, in section 3, we provide an overview of several model variables and assess their strengths and weaknesses for the purpose of delineating convective cold pool boundaries. The insights gained from this investigation help to guide the development of a new cold pool identification and tracking algorithm, which is introduced in section 4. The algorithm described in section 4 is applied to the simulation described in section 2, and the identified cold pools are averaged together to create a composite cold pool. The properties of the composite cold pool are explored in section 5. Finally, conclusions are drawn in section 6.

**Table 1.** RAMS Model Setup, Adapted From *Grant and van den Heever* [2014]

Model Aspect	Setting
Grid	Arakawa C grid $\Delta x = \Delta y = 1 \text{ km}$ ; 550 km $\times$ 200 km domain size $\Delta z$ variable minimum $\Delta z = 100 \text{ m}$ , maximum $\Delta z = 1 \text{ km}$ vertical stretch ratio = 1.05 57 vertical levels; model top $\sim 26 \text{ km}$
Time integration	3 s time step; 16 h simulation duration
Initialization	Horizontally homogeneous thermodynamic and wind profile, averaged from ECMWF YOTC analysis data Initial start time 600 UTC 1 July Random thermal perturbations through lowest 2 km agl, with a maximum magnitude of 1 K at the lowest model level above ground
Surface scheme	LEAF-3 [Walko et al., 2000] 11 soil levels from 0.01 m to 0.5 m below ground Western third of domain: ocean (SST 300 K) Eastern two thirds of domain: evergreen broadleaf tree surface type, sandy clay loam soil type
Boundary conditions	Radiative lateral boundary [Klemp and Wilhelmson, 1978] in zonal direction; periodic in meridional direction Rayleigh friction damping over top six vertical levels ( $\sim 21\text{--}26 \text{ km}$ agl)
Microphysics scheme	Two-moment bulk microphysics [Meyers et al., 1997] Eight hydrometeor classes [Saleeby and Cotton, 2004]
Radiation scheme	Harrington [1997] two-stream, updated every five simulation minutes
Aerosol treatment	Aerosol species: sulfates [Saleeby and van den Heever, 2013] No aerosol sources or sinks Aerosols radiatively active DeMott et al. [2010] ice nucleation parameterization
Turbulence scheme	Smagorinsky [1963] deformation K with stability modification by Hill [1974]; stability modifications by Lilly [1962] used gradually above the boundary layer
Coriolis	No

## 2. Model Setup

This study analyzes cold pools evident within the control simulation of *Grant and van den Heever* [2014]. The simulation was run using the open-source Regional Atmospheric Modeling System (RAMS) (<http://vandenheever.atmos.colostate.edu/vdhp/rams.php>) [Cotton et al., 2003; Saleeby and van den Heever, 2013], coupled to the Land-Ecosystem-Atmosphere-Feedback (LEAF) version 3 land surface model [Walko et al., 2000].

The model configuration is summarized in Table 1. The simulation was designed for the study of tropical sea-breeze convection. Thus, the domain was nonrotating ( $f = 0$ ), and the western one third of the domain had an ocean-type surface, whereas the eastern two thirds of the domain had a tropical rainforest-type surface. The model was initialized with random perturbations to the  $\theta$  field in the lowest 2 km of the domain. The initial horizontally homogeneous (aside from the aforementioned  $\theta$  perturbations) thermodynamic and wind profiles were modified from an average of ECMWF YOTC analysis data and can be found in *Grant and van den Heever* [2014, Figure 1]. There is approximately  $18 \text{ m s}^{-1}$  of vertical wind shear between the surface and 200 hPa and  $5 \text{ m s}^{-1}$  of vertical wind shear between the surface and midtroposphere, where the tops of the cold pool-producing clouds in this study are located. The simulation was initialized at 600 UTC (700 LT) and run for 16 h in order to capture the development of the sea breeze and convection over the course of the day. Model outputs were saved every five simulation minutes. The size of the domain was 200 km (meridional)  $\times$  550 km (zonal)  $\times$  26 km (vertical), and the simulation was run with a horizontal grid spacing of 1 km, and 57 stretched vertical levels with 100 m grid spacing near the surface increasing to 1 km aloft.

Figure 1 shows a snapshot of density potential temperature,  $\theta_p$ , at the lowest model level. Values of  $\theta_p$  are lowest within the oceanic part of the domain and within the sea breeze. Ahead (to the east) of the sea breeze are dozens of convective cold pools at various stages of their life cycles. The present study focuses on the convection that develops ahead of the sea breeze and the cold pools produced by this convection. The sea-breeze identification method of *Grant and van den Heever* [2014] is used to locate the sea-breeze front, and only cold pools forming ahead of the sea-breeze front and more than 50 km from the eastern edge of the domain are analyzed. In the sections that follow, several perturbation quantities are discussed and shown. As in *Grant and van den Heever* [2014], these are defined relative to an average over the part of the domain that extends from 10 km ahead of the identified sea-breeze front location to 50 km from the eastern edge of the domain.

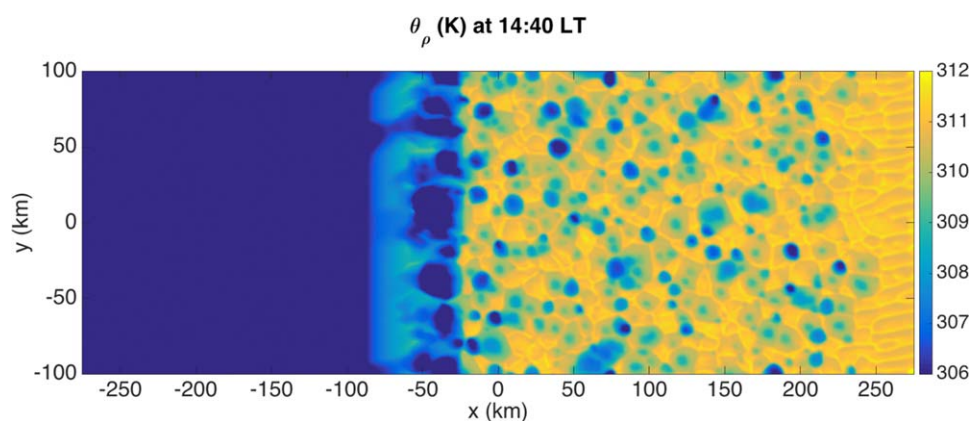


**Figure 1.** Snapshot of the  $\theta_p$  field at the lowest model level,  $z \sim 50$  m. The ocean-land boundary is at  $x \sim -92$  km, and the sea-breeze location is identified to be at  $x \sim -22$  km.

### 3. Choice of Variables to Identify Cold Pools

Several variables have been used to define convective cold pool boundaries and attributes in previous work, both in observations and in models. These include buoyancy [Tompkins, 2001; Grant and van den Heever, 2014, 2016; Seigel, 2014; Feng et al., 2015], along with related metrics such as (virtual or density) (potential) temperature [Addis et al., 1984; Young et al., 1995; Terai and Wood, 2013; Yokoi et al., 2014; Torri et al., 2015] and density [Wilbanks et al., 2015]; equivalent potential temperature  $\theta_e$  [Dawson et al., 2010; Katona et al., 2014; Schlemmer and Hohenegger, 2014]; humidity [Redl et al., 2015]; and winds [Uyeda and Zrnić, 1986; Engerer et al., 2008; Li et al., 2014; Kilpatrick and Xie, 2015; Langhans and Romps, 2015]. In this section we examine several of these variables, along with a few additional ones, and assess each variable's utility for characterizing convective cold pools according to the following criteria:

1. There should exist some physical basis for using this variable to define convective cold pools. Otherwise, it is unlikely to be useful across many types of different cold pool environments.
2. When this variable is plotted, cold pool edges should be apparent and in physically reasonable locations. One physically reasonable location is the density current edge, where there is a characteristic transition between downdrafts (within the density current) and updrafts (in front of the density current) accompanied by a strong gradient in the density potential temperature. Furthermore, when this variable is plotted, it should be possible to distinguish cold pools that collide with one another.
3. It should be possible to locate cold pool edges without the use of arbitrary thresholds. If thresholds must be used, then they should have some physical basis, and the resulting edges should be relatively insensitive to the choice of threshold.

It will be shown that although several variables satisfy some of these criteria, none satisfy all of these criteria. In the discussion that follows, a single, illustrative convective cold pool is examined in terms of several different variables. The evolution of this cold pool is shown in Figure 2. This specific cold pool is particularly "well-behaved" in that it is isolated, approximately circular, and creates robust perturbations to various dynamic and thermodynamic fields. For this reason, its boundaries should be particularly easy to define. Although only a single cold pool is shown, the conclusions that it yields regarding the utility of the different variables are representative of the other cold pools in the simulation. In the figures presented here, this cold pool is shown at multiple times during its lifecycle. The time that is shown most often, which corresponds to Figure 2c, will be defined as  $t = 0$  min, and other times will be defined accordingly. We now consider the strengths and weaknesses of 10 potentially useful variables to identify cold pools.

#### 3.1. Buoyancy

As is noted in Tompkins [2001], buoyancy  $B$  is a natural choice for defining convective cold pools since cold pools act as density currents. Thus, there is a strong physical basis for using buoyancy, as well as related variables such as density potential temperature  $\theta_p$ , to define cold pool boundaries. Since buoyancy is calculated from the density potential temperature, trends in one variable are identical (apart from a multiplicative constant) to trends in the other. The density potential temperature,  $\theta_p$ , and the radial component of the density

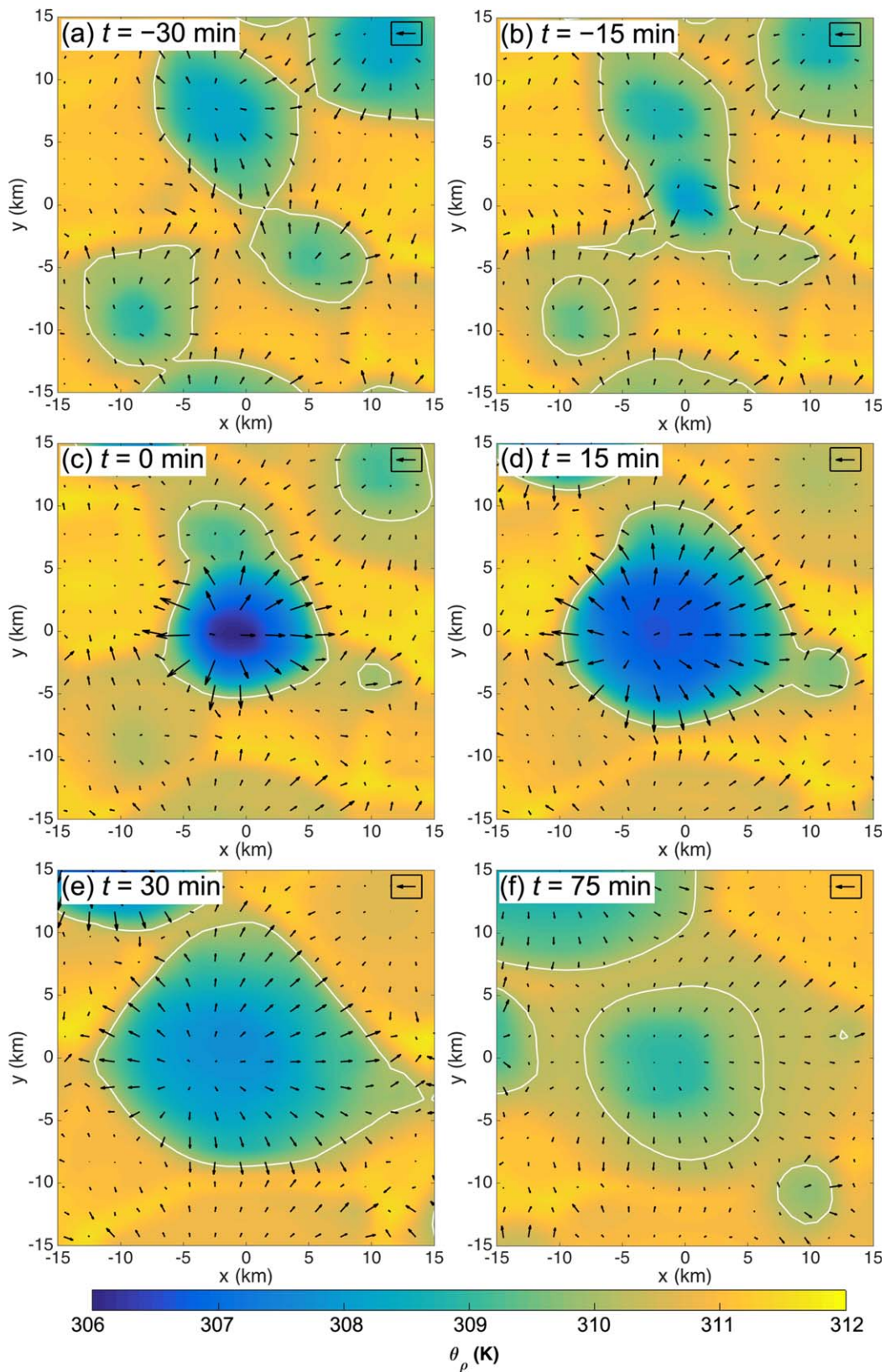


**Figure 2.** Evolution of the  $\theta_p$  field (colors),  $B=0$  contour (white), and horizontal winds (black vectors) at  $z \sim 50$  m for the sample cold pool: (a)  $t = -30$  min; (b)  $t = -15$  min; (c)  $t = 0$  min; (d)  $t = 15$  min; (e)  $t = 30$  min; (f)  $t = 75$  min. Horizontal coordinates are computed relative to the approximate center of the cold pool and thus differ from those in Figure 1. The upper right wind vector in each panel has a magnitude of  $5 \text{ m s}^{-1}$ . Note that the area enclosed by the white  $B=0$  contour decreases from Figure 2e to 2f.

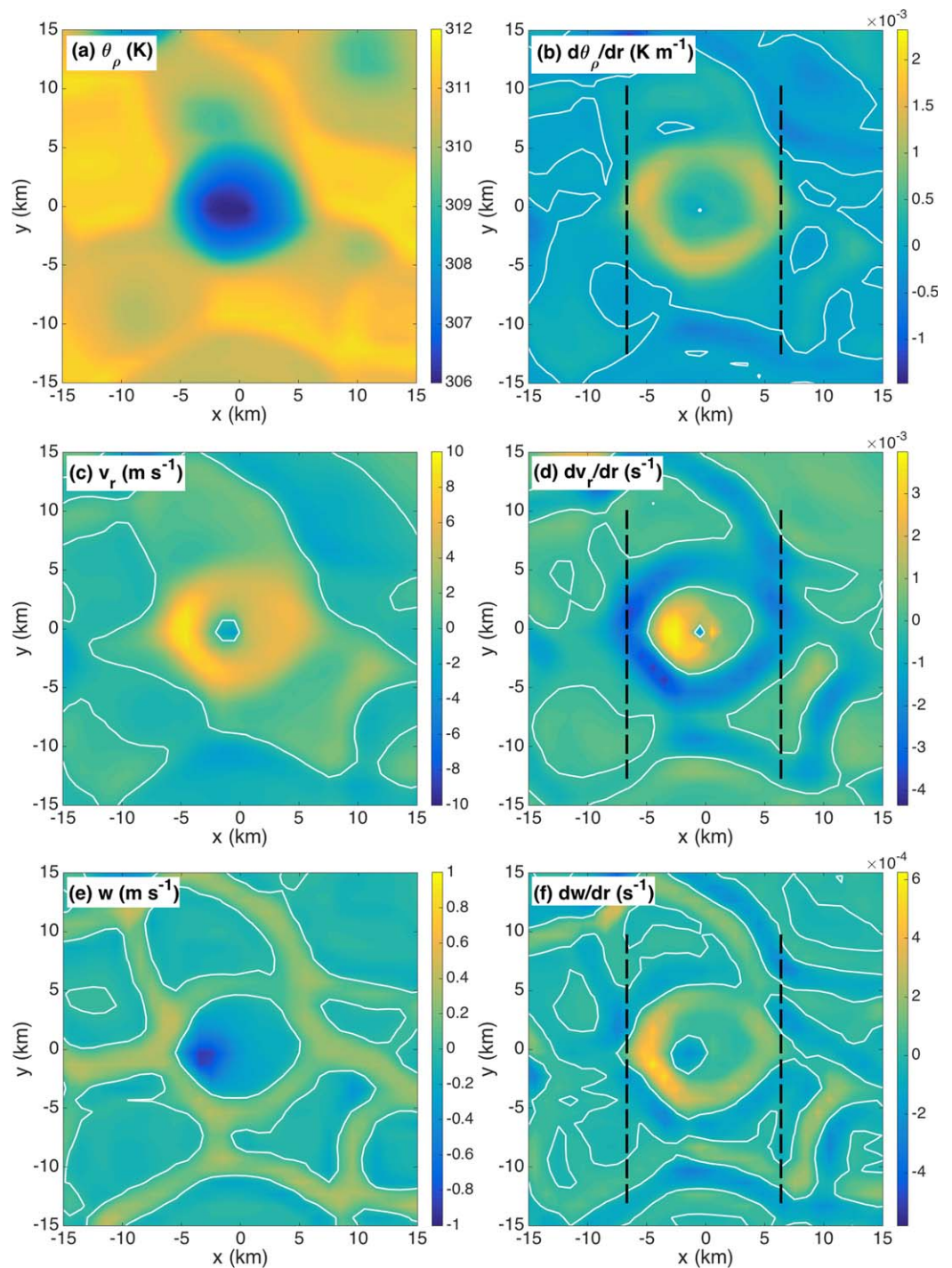


**Figure 3.** Three variables and their radial derivatives at  $t = 0$  min: (a) density potential temperature  $\theta_\rho$  at  $z \sim 50$  m, (b)  $\frac{\partial \theta_\rho}{\partial r}$  at  $z \sim 50$  m, (c) radial velocity  $v_r$  at  $z \sim 50$  m, (d)  $\frac{\partial v_r}{\partial r}$  at  $z \sim 50$  m, (e) vertical velocity  $w$  at  $z = 100$  m, and (f)  $\frac{\partial w}{\partial r}$  at  $z = 100$  m. Zero contours are shown in white. The vertical dashed black lines are shown to facilitate comparison between Figures 3b, 3d, and 3f. Note that the radial gradients in  $v_r$  (dark blue) are located radially outward from the radial gradients in  $\theta_\rho$  and  $w$  (orange).

potential temperature gradient,  $\frac{\partial \theta_\rho}{\partial r}$ , are plotted in Figures 3a and 3b, respectively. The radial derivative is calculated with respect to a cold pool center determined using the method developed in section 4. The  $\frac{\partial \theta_\rho}{\partial r}$  field exhibits a ring of strong positive values as cool density potential temperatures inside the cold pool give way to warmer values outside the cold pool. These strong gradients necessarily occur at the edge of the density current. Therefore, there exists a physical basis for stating that these gradients, and thus any cold pool

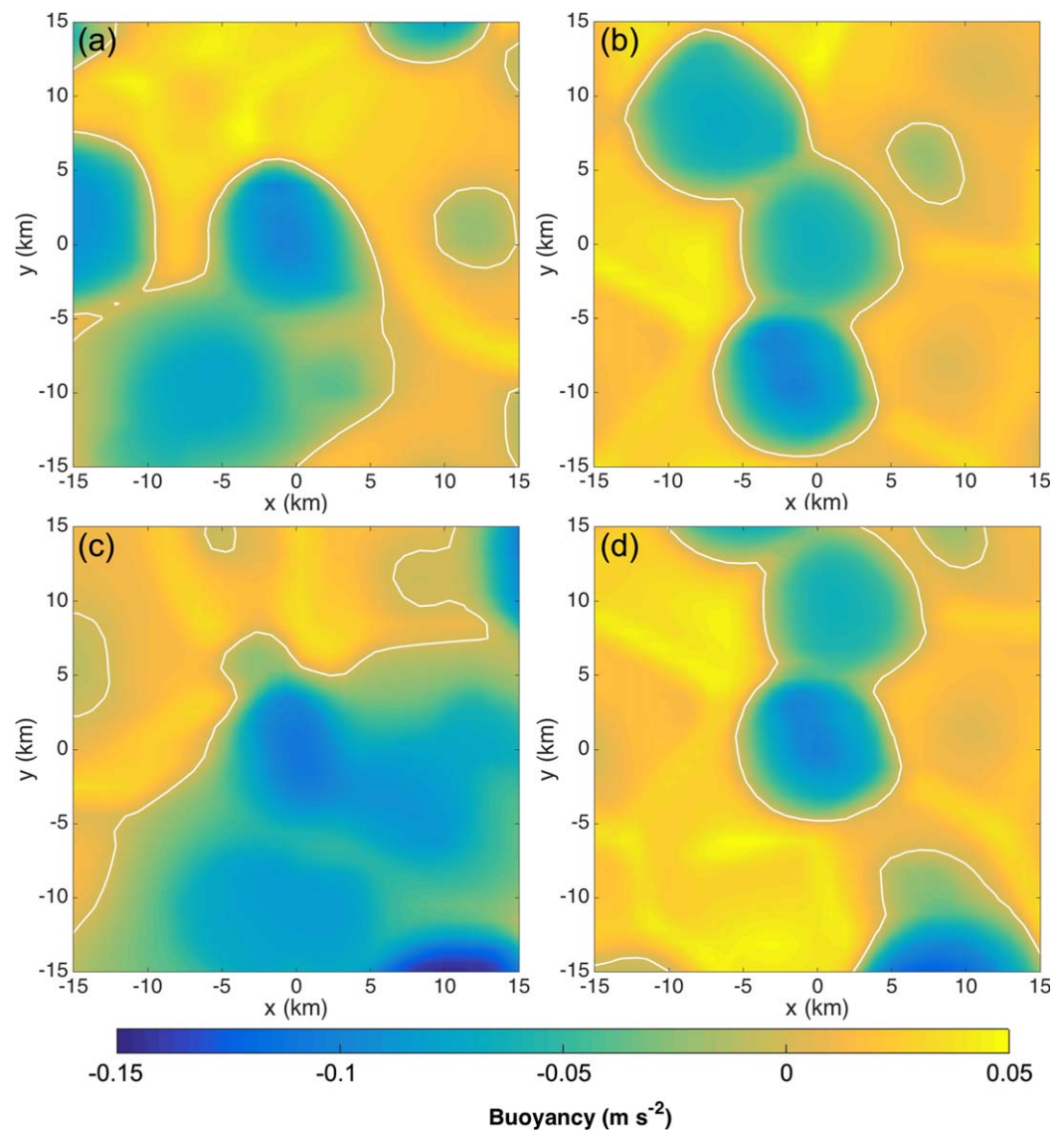


**Figure 4.** Buoyancy field at  $z \sim 50$  m for an assortment of colliding cold pools. The  $B=0$  contour is plotted in white.

boundaries derived from these gradients, are in a physically reasonable location. The discussion that follows will refer to the location of these  $\theta_p$  gradients, which is the location of the edge of the density current, as a *reference location* that can be compared to the locations of cold pool boundaries derived from other variables.

Despite the strengths of the buoyancy field, there are some drawbacks. One drawback is that if the cold pool is defined as a region in which buoyancy is below some given threshold, then the size of the cold pool—according to this definition—will eventually begin to decrease with time as the cold pool dissipates and regions of negative buoyancy disappear, as is shown in Figure 2 for a threshold of  $B=0 \text{ m s}^{-2}$ . If we consider the cold pool boundary to be the location of the gust front, then a decrease in cold pool area would correspond to a retreat of the gust front. Under this interpretation of the boundary of a cold pool, this is not a physical outcome. Gust fronts propagate outward from the center of the cold pool and do not typically retreat. Another drawback of the use of buoyancy lies in the choice of threshold. As discussed in section 1, the definition of buoyancy relies on the specification of a somewhat arbitrary reference state. For this reason, there is no strong physical basis for any particular choice of buoyancy threshold.

Figure 4 shows several scenes that feature colliding cold pools. It is apparent that a simple fixed buoyancy threshold will not suffice to identify the edges of the various cold pools that are evolving in space and time. However, from these scenes it does seem possible to discern the locations of the cold pool boundaries by

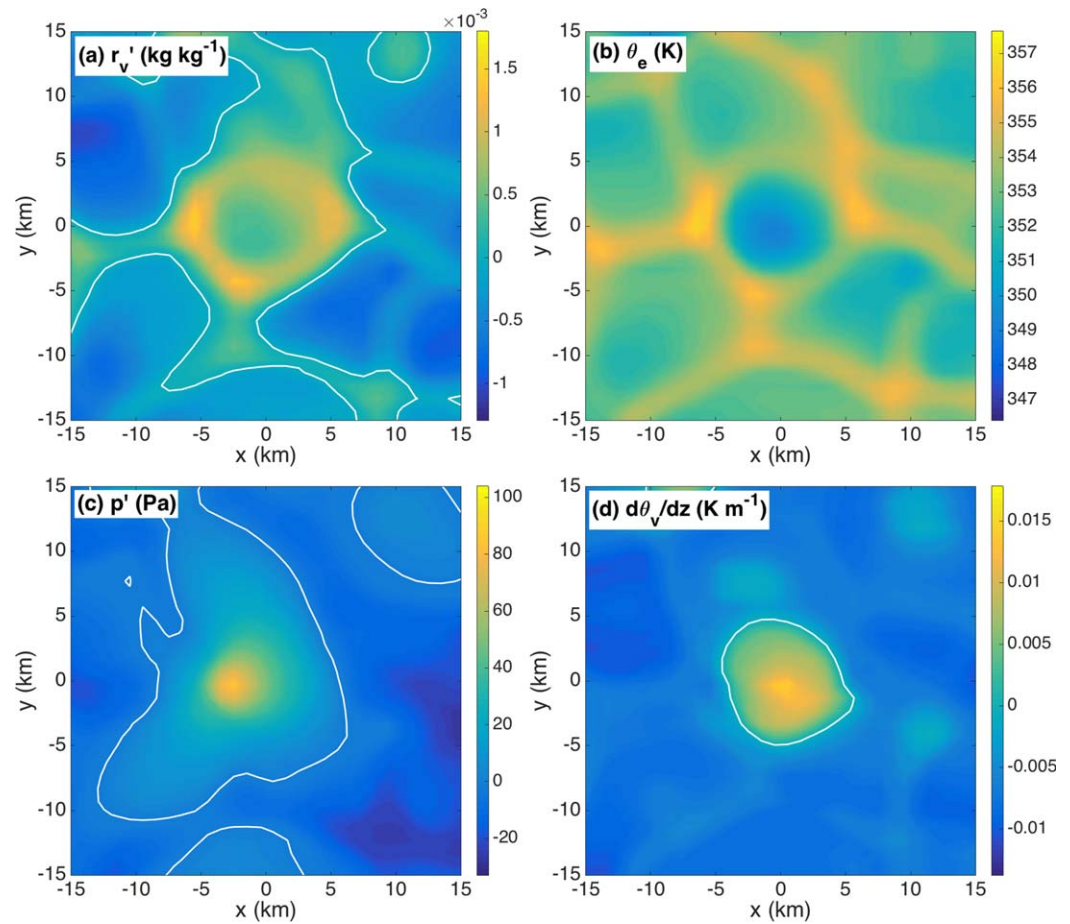


**Figure 5.** Various fields at  $t = 0$  min: (a) perturbation water vapor mixing ratio  $r'_v$  at  $z \sim 50$  m, (b) equivalent potential temperature  $\theta_e$  at  $z \sim 50$  m, (c) perturbation pressure  $p'$  at  $z \sim 50$  m, and (d) static stability  $\frac{\partial \theta_v}{\partial z}$  at  $z \sim 100$  m. Zero contours are plotted in white.

visual inspection (assuming some knowledge on the part of the viewer). Thus, we can state that the buoyancy field does contain information about where the boundaries are. Analysis methods more sophisticated than the application of a uniform threshold may be able to identify the boundaries of colliding cold pools based on the information present in the buoyancy field. This is further investigated in section 4.

### 3.2. Water Vapor Mixing Ratio

In the simulation examined here, convective cold pools are characterized by a ring of enhanced moisture along the periphery of the cold pool surrounding a relatively dry cold pool interior, as is shown in Figure 5a. This structure, however, may be different in other environments. In fact, the time series of dew point temperature in Redl *et al.* [2015, Figure 3c] for cold pools in northwest Africa do not suggest the presence of a dry cold pool interior but rather that cold pool air in such regions may, in fact, be relatively moist throughout. As pointed out in Langhans and Romps [2015], rings of enhanced moisture occur in large part due to surface latent heat fluxes, which themselves depend on surface properties. Furthermore, an arbitrary threshold would be necessary in order to use water vapor mixing ratio to determine convective cold pool boundaries. For these reasons, water vapor mixing ratio appears to be ill suited for this task.

### 3.3. Equivalent Potential Temperature

Although equivalent potential temperature  $\theta_e$  has many attractive qualities, such as its conservation under moist pseudoadiabatic processes, there is limited physical basis for using it to define convective cold pool boundaries because it is not directly related to density. In fact, the boundaries that might be obtained using  $\theta_e$  do not necessarily match those that would be obtained using buoyancy or  $\theta_\rho$ . This is due to the role that water vapor has in the calculation of  $\theta_e$ . As discussed in section 3.2, the simulation examined here exhibits rings of enhanced water vapor at the periphery of convective cold pools. These rings of enhanced water

vapor, which occur in regions of negatively buoyant air, raise the local values of  $\theta_e$  along cold pool peripheries such that cold pools appear to be smaller in the  $\theta_e$  field than in the  $\theta_\rho$  field, as can be seen when comparing Figure 5b with Figure 3a. The gradients in  $\theta_e$  (not shown) are located radially inward of the reference location discussed in section 3.1. This means that cold pools identified based on the  $\theta_e$  field may be too small compared with those based on the  $\theta_\rho$  field, and caution should be used when using  $\theta_e$  to define convective cold pool boundaries.

### 3.4. Perturbation Pressure

There does exist a physical basis for defining convective cold pools based on perturbation pressure. Cold pools act as density currents, and by the hydrostatic relation, the increased density associated with convective cold pools should be accompanied by a positive pressure perturbation. However, the warm air aloft associated with cold pools' parent cloud systems creates a negative pressure perturbation, which can counteract some of the positive pressure perturbation associated with the cold pool. Furthermore, as Figure 5c shows, the perturbation pressure field does not exhibit any clear edges (i.e., no sharp gradients). Thus, the perturbation pressure field is not well suited for determining convective cold pool boundaries.

### 3.5. Static Stability

When downdraft air reaches the ground, it spreads out, coating the surface with cool air to form a cold pool. This air has a lower virtual potential temperature than the air above it, and thus there exists a layer of stable stratification. This is the physical basis for considering the use of static stability,  $\frac{\partial\theta_v}{\partial z}$ , to define convective cold pools. A potential threshold for defining the boundary of convective cold pools is  $\frac{\partial\theta_v}{\partial z}=0$ . This threshold has some physical significance as the threshold for absolute static stability. As Figure 5d shows, the near-surface static stability field does exhibit large gradients. However, these gradients do not necessarily occur in the reference location discussed in section 3.1. The turbulence associated with the cold pool gust front may prevent stable stratification along the periphery of the cold pool. Furthermore, as was the case with the buoyancy field, the cold pool area defined by a given static stability threshold tends to decrease as the cold pool dissipates (not shown). This result is unphysical for the same reasons discussed in section 3.1. Finally, the usefulness of static stability for defining convective cold pool boundaries may depend on model grid spacing near the surface, as well as the particular situation, e.g., whether the ambient air is already stably stratified. For these reasons, we hesitate to use static stability to define convective cold pool boundaries.

### 3.6. Radial Velocity

As downdraft air reaches the surface, it spreads out, forming a density current propagating in the radially outward direction. Thus, there is a physical basis for defining convective cold pools according to the radial velocity field. Indeed, the terms *outflow* and *gust front*, both associated with cold pools, refer to radially outward pointing winds. Furthermore, as Figure 3d shows, the radial velocity field exhibits a strong radial gradient as the strong radial winds of the gust front give way to the weaker and/or directionally different ambient flows outside the cold pool. There are additional potential advantages of using the radial velocity  $v_r$  to define convective cold pool boundaries. One potential advantage is that there exists a physically based threshold of  $0 \text{ m s}^{-1}$  that might be used to delineate cold pool boundaries, although it should be noted that turbulent motions interfere with the use of this threshold. Another potential advantage is that the boundaries between colliding cold pools become immediately apparent in the  $v_r$  field: from the perspective of some given cold pool, the radial outflow associated with an adjacent cold pool will be directed radially inward. The boundary between the given cold pool and the adjacent one would simply be the zero contour of  $v_r$ .

In practice, unfortunately,  $v_r$  does not succeed in identifying cold pool boundaries. Even though a physically based threshold exists, it only works when the ambient flows are directed radially inward. Moreover, the raw  $v_r$  field does not yield discrete boundaries between colliding cold pools (Figure 6). Attempts to identify boundaries between colliding cold pools using the more sophisticated methods of section 4 with  $v_r$ , while generally successful, appear to be no more successful than attempts based on buoyancy or  $\theta_\rho$  (not shown). There exist other drawbacks as well. One is that a cold pool center must be specified in order to calculate the radial component of the wind. Another is that boundaries obtained using  $v_r$  are not quite in the reference location established in section 3.1. As shown in Figures 3c and 3d, the region of enhanced  $\frac{\partial v_r}{\partial r}$  lies radially outside the region of enhanced  $\frac{\partial\theta_\rho}{\partial r}$ . This result is typical of convective cold pools in this simulation. Thus, cold pools identified using  $v_r$  will be larger than those identified using buoyancy or  $\theta_\rho$ .

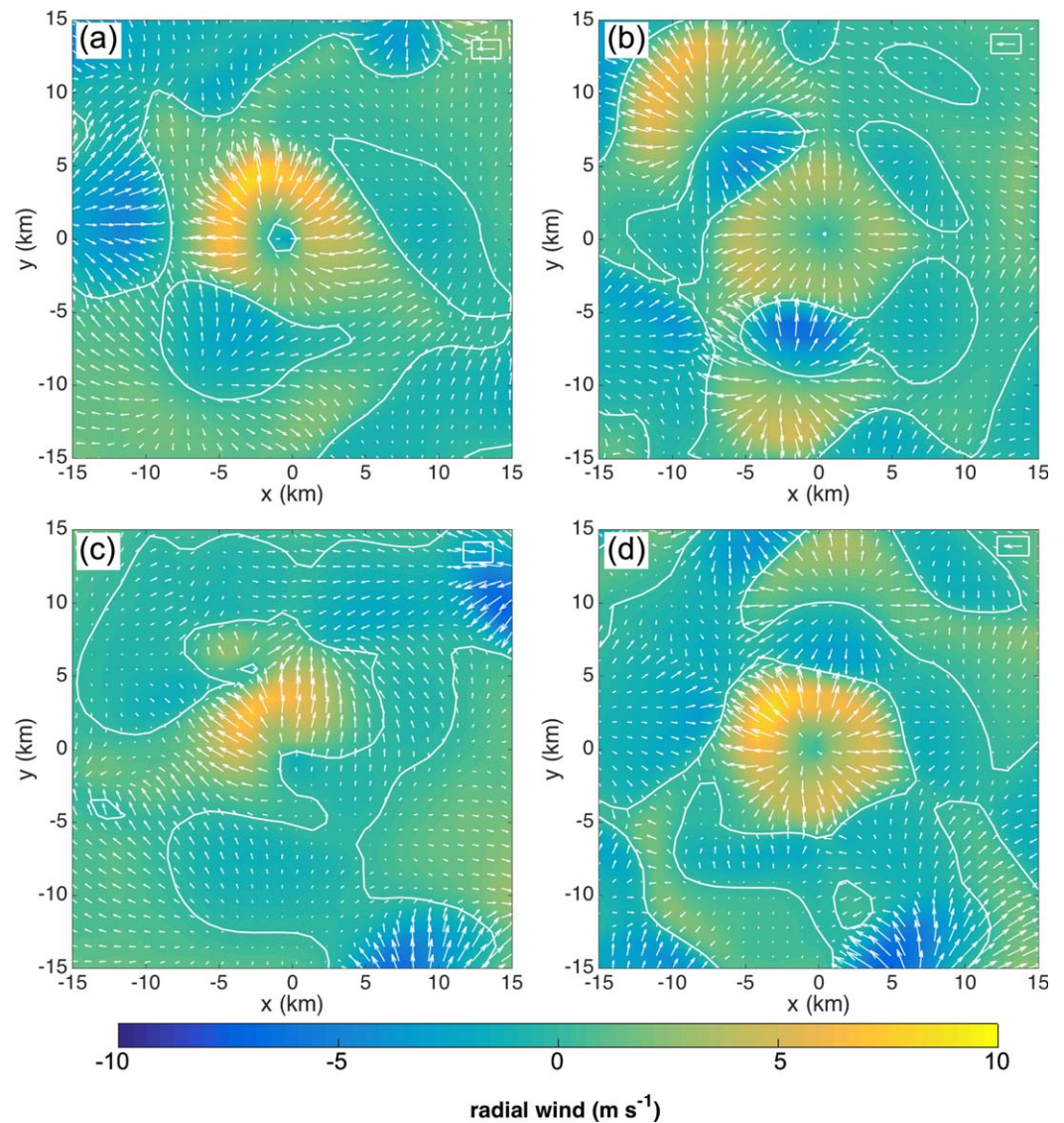


**Figure 6.** Radial velocity  $v_r$  (colors) and horizontal wind vectors (white arrows) at  $z \sim 50$  m for the colliding cold pool scenes shown in Figure 4. In each panel, the radial velocity is computed relative to the approximate center of the centermost cold pool in the scene. The  $v_r = 0$  contour is shown in white. The leftward pointing arrow in the upper right corner of each panel has a magnitude of  $5 \text{ m s}^{-1}$ .

### 3.7. Vertical Velocity

Convective cold pools are spawned by downdrafts, and along cold pool edges, convergence of the horizontal wind field yields rising motion. The latter motion is referred to by Goff [1976] as the *prefrontal updraft*. Thus, there does exist a physical basis for defining cold pool boundaries in terms of vertical velocity. There is a transition from downdrafts inside the cold pool to updrafts outside the cold pool. This transition serves as physical justification for a vertical velocity threshold of  $0 \text{ m s}^{-1}$ . Furthermore, there are strong gradients in vertical velocity associated with this transition. These gradients are located in approximately the same location as the gradients in buoyancy and are thus in the reference location discussed in section 3.1 (Figures 3e and 3f). However, the signature ring of downdrafts surrounded by updrafts only exists in areas and during times in which the cold pool is actively expanding. Factors such as turbulence may interfere with this signature pattern as well. In an examination of the near-surface vertical velocity field for many convective cold pools within the simulation (not shown), it is often the case that the zero contour in vertical velocity does not completely circumscribe the cold pool. In these cases there is no closed contour. Based on this result, we have concluded that vertical velocity is not the best option for identifying convective cold pool boundaries.

### 3.8. Surface Latent Heat Flux

In *Tompkins* [2001], convective cold pools are observed to be collocated with large enhancements in the surface latent heat flux. It is therefore worth exploring whether surface latent heat fluxes can be used to define convective cold pool boundaries. In the idealized simulation of *Tompkins* [2001], there are two factors that allow enhanced surface latent heat fluxes in convective cold pools: the relatively dry cold pool interior (see section 3.2) into which enhanced evaporation may occur, and the strong winds associated with the cold pool outflow (see section 3.6). In the simulation examined in the present work, we do not observe enhanced latent heat fluxes throughout the convective cold pools; in fact, the interiors exhibit markedly decreased latent heat fluxes (Figure 7a). These regions of decreased latent heat fluxes are due in part to relatively calm winds near the center of the cold pool, and in part to the enhanced relative humidity (which itself is due to cool temperatures rather than enhanced mixing ratios). However, the major factor in suppressing latent heat fluxes near the center of the cold pool appears to be shading of shortwave radiation by the cold pool's parent cloud system (Figure 7b). This response was also observed by *Schlemmer and Hohenegger* [2016]. In regions that are shaded, there is less incoming energy available with which to perform evapotranspiration, and thus less latent heat flux. Unlike the simulation of *Tompkins* [2001], the simulation analyzed in the present work uses an interactive radiation scheme, and so shading—and therefore the effects of shading on surface fluxes—can be realized. The heterogeneities in the surface latent heat flux field, as well as the lack of a physically meaningful threshold value, make it a poor choice of variable for determining convective cold pool boundaries.

### 3.9. Surface Sensible Heat Flux

It is noted in *Tompkins* [2001] that the boundary layer temperatures and surface sensible heat fluxes are “almost perfectly negatively correlated.” *Tompkins* [2001] uses a fixed-sea surface temperature (SST)

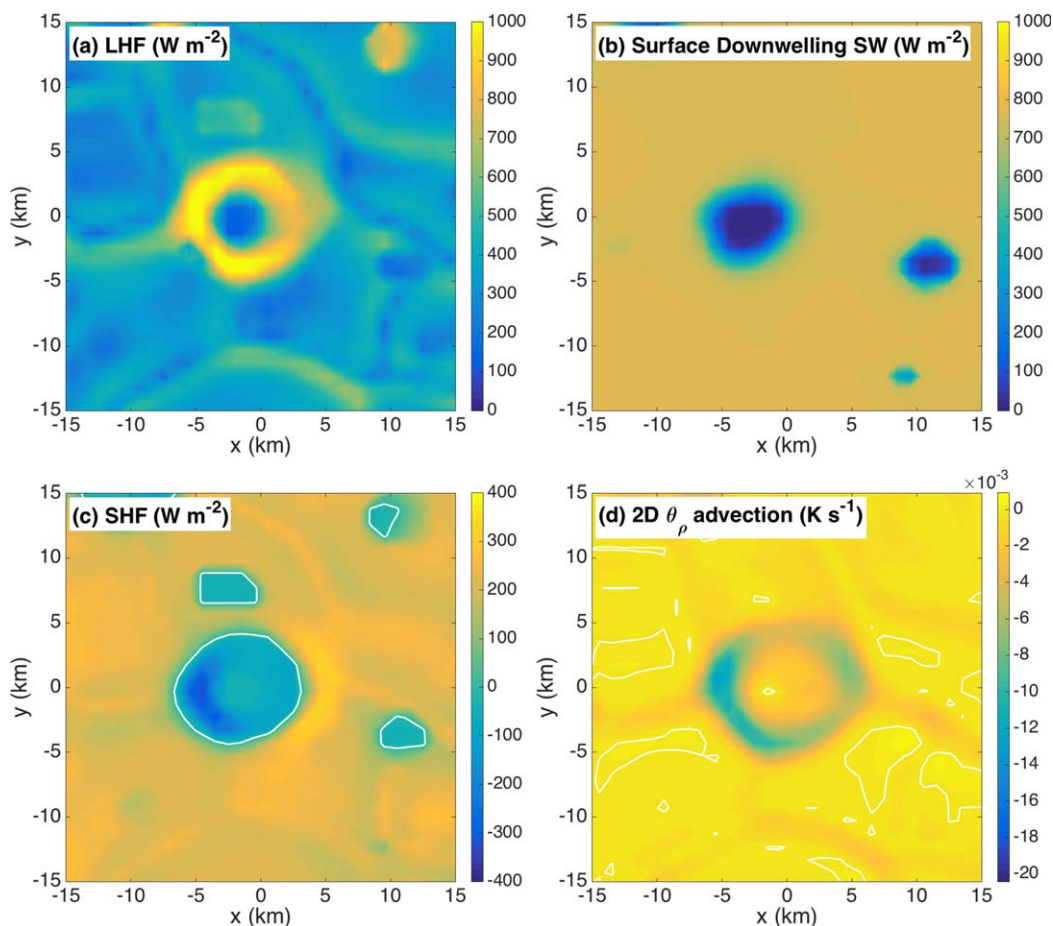


**Figure 7.** Various fields at  $t = 0$  min: (a) surface latent heat flux, (b) downwelling shortwave radiation at the surface (c) surface sensible heat flux, and (d) horizontal density potential temperature advection  $-\bar{v}_H \cdot \bar{\nabla}_H \theta_\rho$  at  $z \sim 50$  m. Zero contours are shown in white.

surface. Where boundary layer temperatures are much lower than the SST, there is a larger temperature differential, and thus surface sensible heat fluxes are enhanced. Surface sensible heat fluxes are enhanced further by the presence of gusty cold pool winds. Thus, there appears to be a physical basis for defining convective cold pools in terms of the surface sensible heat fluxes. However, as discussed in the previous section, in the simulation analyzed in the present work, there is an interactive surface model. Therefore, the patterns in the sensible heat flux field are potentially more realistic. Although there are strong gradients in the surface sensible heat flux field (Figure 7c), these gradients are associated not with the temperature gradients of the cold pool, but rather with regions in which precipitation has soaked the ground, thereby lowering the surface temperature. Thus, the edges are not in the reference location established in section 3.1, and surface sensible heat flux is not a suitable variable for determining convective cold pool boundaries.

### 3.10. Density Potential Temperature Advection

One field that has received less attention in the literature is the horizontal density potential temperature advection,  $-\vec{v}_H \cdot \vec{\nabla}_H \theta_\rho$  (where  $\vec{v}_H$  is the horizontal velocity vector and  $\vec{\nabla}_H$  is the horizontal gradient operator), which is displayed in Figure 7d. This field shows where cool air is advected into warmer regions as the cold pool spreads out. Thus, this field illustrates the active edge of the cold pool. There is a ring of strong negative values around the periphery of the cold pool, where cooler air is arriving. There is thus a strong physical basis for using this field to define convective cold pools. One drawback to using this field is that an arbitrary threshold must be applied. The field is almost uniformly negative, and so a physically based threshold of  $0 \text{ K s}^{-1}$  will not work. Nevertheless, if one is willing to apply an arbitrary threshold, then this field might prove to be a useful field for identifying convective cold pool boundaries.

## 4. Algorithm for Cold Pool Identification and Tracking

### 4.1. Algorithm Development

The use of spatial derivatives can allow us to minimize the use of arbitrary thresholds because new physically based thresholds may emerge. When spatial derivatives are used, there is an inherent physical meaning in a threshold of zero. Where the first derivative equals zero, there is typically a maximum or minimum. Where the second derivative equals zero, there is typically an inflection point.

Consider an idealized circular, axisymmetric cold pool in which the inside of the cold pool has a uniform cool temperature and the environment has a uniform warmer temperature, as shown in Figure 8. The inflection point of the  $\theta_\rho(r)$  curve in Figure 8a, which is also the point at which  $\frac{\partial^2 \theta_\rho}{\partial r^2} = 0$  in Figure 8e, appears subjectively to be a suitable choice of cold pool boundary; it aligns with the region in which the first derivative,  $\frac{\partial \theta_\rho}{\partial r}$  (Figure 8c), is greatest and hence the region in which the gradients are greatest. This reasoning extends to nonidealized, nonaxisymmetric cold pools as well, provided that their shapes are nearly circular. Figures 8b, 8d, and 8f illustrate these quantities,  $\theta_\rho$ ,  $\frac{\partial \theta_\rho}{\partial r}$ , and  $\frac{\partial^2 \theta_\rho}{\partial r^2}$ , for the cold pool examined in section 3, where the radial derivatives are computed relative to a cold pool center determined according to the method described later in this section. The patterns of positive and negative values follow the idealized profiles closely, and the  $\frac{\partial^2 \theta_\rho}{\partial r^2} = 0$  contour forms a suitable cold pool boundary.

Several variables were tested in addition to  $\theta_\rho$ ; some additional examples are shown in Figure 9. It was determined that  $\frac{\partial^2 \theta_\rho}{\partial r^2}$  most reliably yielded closed contours in subjectively reasonable locations. Compared to vertical velocity (Figure 9b), which performs well in the example shown, it was found that  $\frac{\partial^2 \theta_\rho}{\partial r^2}$  yielded closed contours earlier in the cold pool lifecycle, perhaps due to the effects of turbulence on the vertical velocity field. One alternative to using the second radial derivative of  $\theta_\rho$  is to use the horizontal Laplacian of  $\theta_\rho$  (Figure 9d). These two options are similar in formulation, and in the presence of axisymmetry, the horizontal Laplacian simplifies to the second radial derivative. One advantage of the horizontal Laplacian is that it can be calculated without first determining a cold pool center. However, it is observed that the horizontal Laplacian does not yield clean, circular contours surrounding cold pools, as is the case for the cold pool shown (compare Figure 8f to Figure 9d). This difference results from the varying response to numerical noise. The contours in  $\frac{\partial^2 \theta_\rho}{\partial r^2}$  are susceptible only to the radial component of gradients arising from numerical noise, whereas the contours in the horizontal Laplacian of  $\theta_\rho$  are susceptible to both directional components of gradients arising from such noise.

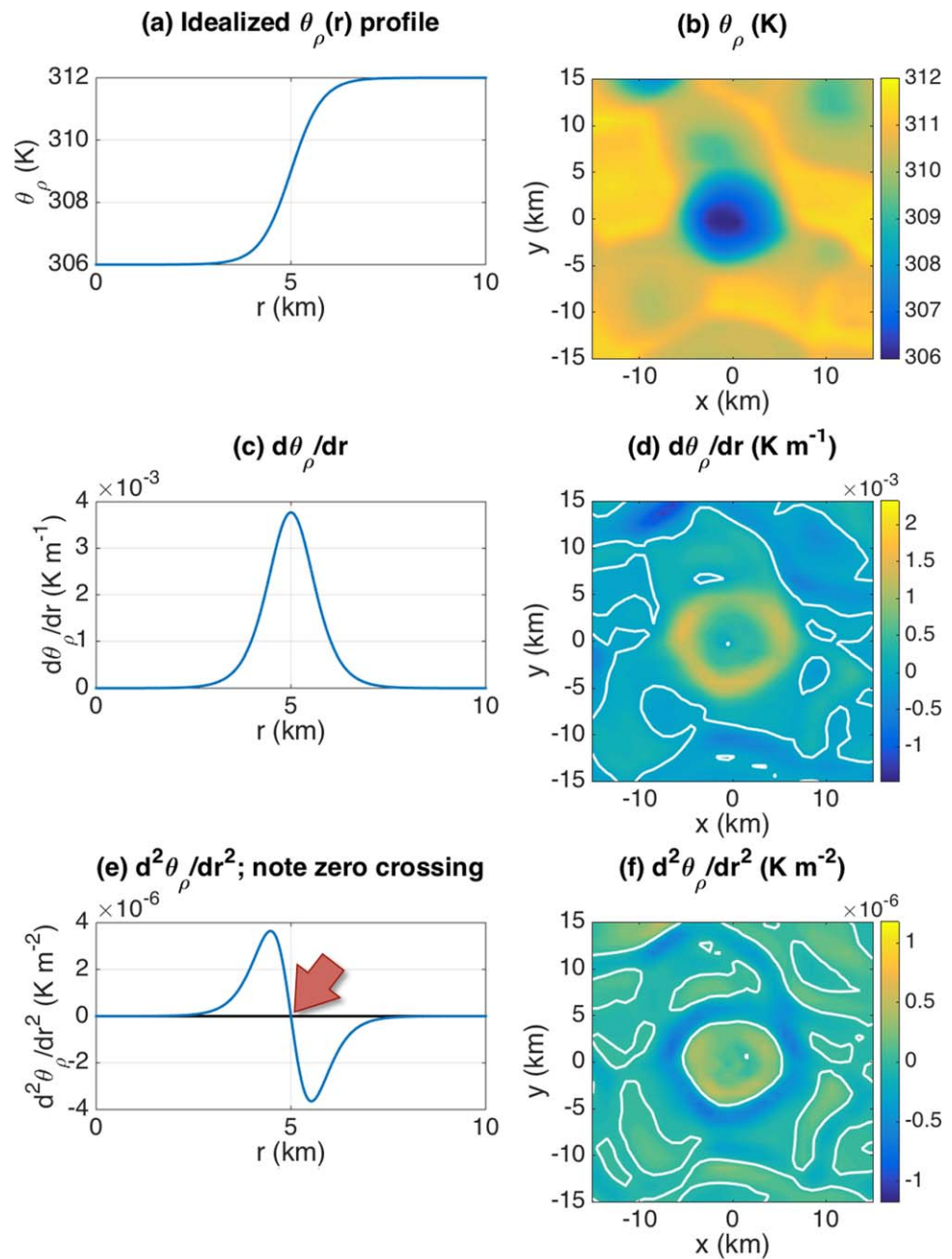


**Figure 8.** Illustration of the reasoning behind using the second radial derivative: (a, b)  $\theta_\rho$ , (c, d)  $\frac{\partial \theta_\rho}{\partial r}$ , and (e, f)  $\frac{\partial^2 \theta_\rho}{\partial r^2}$ . The left panels show an idealized  $\theta_\rho(r)$  profile; the right panels show the cold pool examined earlier at a height of  $z \sim 50$  m. Zero contours are in white.

The specific procedure constituting the cold pool identification and tracking algorithm will now be described. Before we can calculate the second radial derivative of the  $\theta_\rho$  field, we must first identify a cold pool center. However, before we can identify a cold pool center, we must first identify areas of interest where cold pools are likely to be located. Since cold pools are spawned by precipitating clouds, we first identify areas of interest based on the surface rainfall rate. Specifically, areas of interest are defined as contiguous regions in which the surface rainfall rate exceeds some threshold value. Each area of interest corresponds to one potential cold pool. Unfortunately, an arbitrary threshold rainfall rate must be chosen here. A threshold of  $1 \text{ mm h}^{-1}$  is used. This threshold is somewhat more permissive than the  $2 \text{ mm h}^{-1}$  threshold for penetrating downdrafts determined by *Barnes and Garstang* [1982] and used by *Young et al.* [1995], but it is of the same order of magnitude. Areas of interest are contiguous regions where the surface rainfall rate

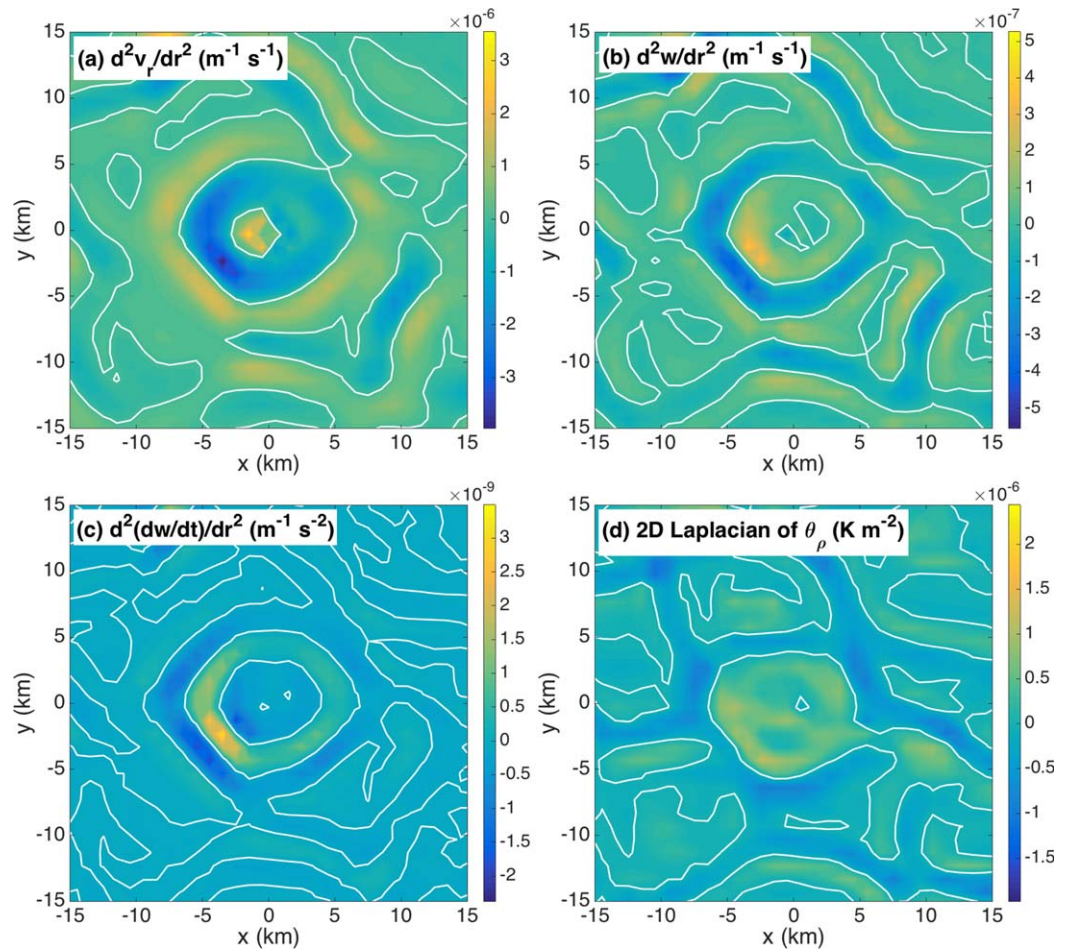


**Figure 9.** Alternative second-order derivatives that were considered for identifying cold pool edges, all at  $t = 0$  min: (a)  $\frac{\partial^2 v}{\partial r^2}$  at  $z \sim 50$  m, (b)  $\frac{\partial^2 w}{\partial r^2}$  at  $z \sim 100$  m, (c)  $\frac{\partial^2}{\partial r^2} \left( \frac{\partial w}{\partial t} \right)$  at  $z \sim 100$  m, and (d)  $\nabla_H^2 \theta_\rho$  at  $z \sim 50$  m. Zero contours are shown in white.

meets or exceeds the  $1 \text{ mm h}^{-1}$  threshold, where pixels are defined as contiguous if they share an edge, but not if they only share a corner (i.e., four connectivity). For purposes of this processing step, any “holes,” i.e., pixels below the  $1 \text{ mm h}^{-1}$  threshold embedded within a region of pixels meeting or exceeding the threshold, are filled in. Then, any regions of area less than  $8 \text{ km}^2$  (eight square-kilometer pixels) are discarded in order to ensure that only robust rainy regions are selected. The centroid of each region is then calculated.

The centroid of each region of contiguous rainy pixels is taken to be the center of a possible cold pool. There is typically some delay between the appearance of a rainy region and the emergence of the cold pool it spawns, at least within the near-surface  $\theta_\rho$  field. Therefore, the next step of the cold pool identification process is applied to the thermodynamic fields 10 min following the identification of the respective rainy regions.

In the next step, convective cold pool boundaries are located as described above using the second radial derivative of density potential temperature,  $\frac{\partial^2 \theta_\rho}{\partial r^2}$ , where the radial coordinate is defined with respect to the centroid of the corresponding rainy region. First, each rainy region’s centroid is computed, and the radial derivatives of  $\theta_\rho$  are calculated accordingly. Then, contiguous regions are identified in which  $\frac{\partial^2 \theta_\rho}{\partial r^2} > 0$ , and any “holes” in these regions are filled in. The boundary of the cold pool may then be chosen from the boundaries of these regions (for instance, from among the various white contours in Figure 8f). A region’s boundary will be chosen if the boundary meets the following criteria:

1. If there are multiple regions, then the region with the centroid that is closest to that of the original rainy region is selected. Furthermore, the distance between this region’s centroid and that of the original rainy region must be less than or equal to the equivalent diameter of the original rainy region, where the

equivalent diameter is defined as the diameter of a circle whose area equals that of the original rainy region.

2. The selected region must occupy at least 90% of the original rainy region's pixels, and the original rainy region (which is typically smaller) must occupy at least 25% of the region's pixels.
3. The region's aspect ratio (the ratio of its minor axis to its major axis) must be greater than or equal to 0.7, and its convexity ratio (also termed *solidity*: the ratio of the object's area to that of its convex hull, which is the smallest convex shape that can contain the object; both terms are defined in Fisher et al. [2014]) must be greater than or equal to 0.8. These specifications ensure that the region is approximately circular and prevent contours with highly irregular shapes uncharacteristic of tropical cold pools from being chosen. Even though cold pools with aspect ratios lower than 0.7 are filtered out, the method of determining cold pool edges based on the zero contour of  $\frac{\partial^2 \theta_p}{\partial r^2}$  has been tested and found to perform well at finding the boundaries of highly elongated, elliptical cold pools with aspect ratios below 0.35 (not shown). Furthermore, adequate performance has been obtained when the cold pool center used to calculate radial derivatives has been displaced by more than 4 km (not shown). Therefore, the use of radial derivatives should not be viewed as a significant limitation in terms of the types of cold pools that can be identified.

If no contiguous region meets all of the above criteria, then the boundary remains undefined, and the original rainy region is discarded. If a region does meet all of the above criteria, then its boundary is taken to be the boundary of the cold pool, and its centroid is taken to be the centroid of the cold pool for all further calculations.

Cold pools are identified at each output time independently of other output times. However, the tracking of cold pools over time is a powerful tool that can be used to probe the cold pool life cycle. Thus, after this identification step, cold pools are tracked between successive output times. Each cold pool at output time  $t$  is compared to the cold pools at output time  $t + 1$ . In order to find a match between the cold pool at time  $t$  and one of the candidate cold pools at time  $t + 1$ , the following criteria must be met:

1. If there are multiple candidate cold pools at time  $t + 1$ , then this candidate cold pool's centroid must be closest to that of the original cold pool at time  $t$ . Furthermore, the distance between the centroids must be no larger than the equivalent radius (the radius of a circle of equivalent area) of the original cold pool at time  $t$ .
2. This cold pool must occupy at least 50% of the original cold pool's pixels, and vice versa.

For the purposes of the present work, the tracking of cold pools over time is only used to prevent the overrepresentation of particular cold pools within the data utilized to generate statistics about cold pool attributes. Tracking provides information regarding how many times a particular cold pool has been identified. The analyses that follow use the information that is collected at the *first* output time at which each cold pool is identified.

Composites are constructed so as to capture the "average" structure and evolution of cold pools when a large ensemble of individual cold pools is present in a simulation. In order for composites to be constructed, cold pools must be "aligned" in time and space. Cold pools are aligned in time according to the first output time at which each cold pool is identified by the cold pool identification algorithm. They are aligned in space according to their centroids. Data are then interpolated onto a cylindrical polar grid with dimensions of  $\Delta r = 1$  km and  $\Delta \phi = \frac{2\pi}{180}$  rad. Radial profiles are then constructed for each cold pool at each height by averaging the interpolated data across  $\phi$ . Composites may then be constructed for any set of cold pools by averaging the radial profiles.

These composites, when constructed for a variety of variables, capture the mean structure of an ensemble of cold pools. If it is further assumed that cold pools are approximately stationary, then the mean evolution can also be captured by projecting cold pool centroids forward and backward across output times (e.g., to 15 min after each cold pool was first identified) and constructing composites at those times according to the same procedure. It is assumed that the centroid remains stationary over time. This compositing approach is similar to that of Tompkins [2001], which also constructed composite radial profiles, albeit based upon "handpicked" cold pools rather than objectively identified ones.

#### 4.2. Algorithm Performance

Figure 10 shows the algorithm performance for an array of convective cold pools from within the simulation described in section 2. For a variety of convective cold pool strengths and shapes, the algorithm

yields subjectively reasonable boundaries that align with the gradients in  $\theta_p$ . Figures 11a–11d show the performance of the algorithm for the scenes of colliding cold pools discussed in section 3, and Figure 11e shows the algorithm performance for the main cold pool discussed in this and the previous section. The algorithm is able to find suitable boundaries for all of the cold pools shown in Figures 10 and 11a–11e. This is not always the case. For example, Figure 11f shows a case in which a new cold pool forms along the periphery of an existing cold pool. In this case, the new disturbance ends up as part of the existing disturbance when the  $\frac{\partial^2 \theta_p}{\partial r^2} = 0$  contour is plotted. The algorithm has other limitations; these are discussed in section 6.

### 4.3. Comparison to Other Methods

In order to evaluate the performance of the algorithm developed here (“new algorithm”) in the context of other cold pool identification methods described in the literature, we have analyzed the model output using both the *Tompkins* [2001] (“Tompkins”) and *Gentine et al.* [2016] (“Gentine”) algorithms. It should be noted that the Gentine algorithm is similar to the Tompkins algorithm, except that a more sophisticated approach (k-means) is utilized to determine the threshold (as opposed to the Tompkins algorithm, which utilizes a user-specified threshold) and virtual temperature is used instead of buoyancy. The result is shown in Figure 12. The boundaries generated by all three methods have been rounded to the nearest grid cell for ease of plotting, resulting in a “blocky” appearance.

One difference in the performance of the new algorithm and that of the Tompkins and Gentine algorithms is that the latter two algorithms are more likely to identify regions of connected cold pools as single cold pools, whereas the new algorithm is better able to distinguish between connected cold pools. This is demonstrated, for example, by cold pool cluster A and the collection of cold pools immediately to the east of B in Figure 12. In the case of cluster A, both the Tompkins algorithm and the Gentine algorithm identify a single region. The Tompkins algorithm also includes as part of this region an additional cold pool to the north-east. By contrast, the new algorithm discerns multiple discrete cold pools. Recall that the new algorithm only identifies regions where there has been recent rainfall, which is why the more mature cold pool containing most of cluster A’s area is not identified by the new algorithm. For the collection of cold pools immediately to the east of B in Figure 12, the Tompkins algorithm identifies a single region, whereas the Gentine and new algorithms both identify three discrete cold pools.

There are also differences between the new algorithm and the Tompkins and Gentine algorithms in terms of which regions are identified as cold pools. The Tompkins and Gentine algorithms both identify numerous regions that are not identified by the new algorithm. This is to be expected, given that the new algorithm only identifies cold pools in the early stages of their life cycle, when it is still or recently has been (within 10 min) raining. Since individual cold pools typically expand in area over time, it might be expected that the cold pools identified only by the Tompkins and Gentine algorithms will primarily be large regions. However, these algorithms also identify several small regions that the new algorithm does not identify, such as those in the vicinity of C in Figure 12. In these cases, the Tompkins and Gentine algorithms are indeed identifying mature, dissipating cold pools, but they are only identifying the boundaries of the cool wet patches (see section 5.2) within these cold pools’ interiors, rather than identifying the boundaries that represent the full outward extent of the dissipating cold pools. For this reason, when applied to this simulation, the Tompkins and Gentine algorithms tend to overestimate the number of the smallest cold pools and underestimate the number of the largest, oldest cold pools. The new algorithm also underestimates the number of large, dissipating cold pools when applied at only a single output time (as has been done for this comparison of algorithms), but this is by design. The new algorithm focuses on smaller, newer cold pools and does not attempt to identify the boundaries of larger, older cold pools without information from the earlier output times when these older cold pools were first identified. When multiple output times are used in the analysis, information from earlier output times is used to analyze older cold pools at later output times, and thus the underestimates of larger, older cold pools are no longer evident. Indeed, in the section that follows, a full life cycle analysis is presented.

To summarize the comparison between these different methods, the Tompkins and Gentine algorithms often characterize clusters of cold pools as single cold pools, whereas the new algorithm is often able to identify and track individual cold pools within such clusters. The Tompkins and Gentine algorithms also misidentify larger, older cold pools as small cold pools due to the wet patch phenomenon described in section 5.2, whereas the new algorithm, rather than identifying them anew during the late stages of their life cycle, tracks these cold pools

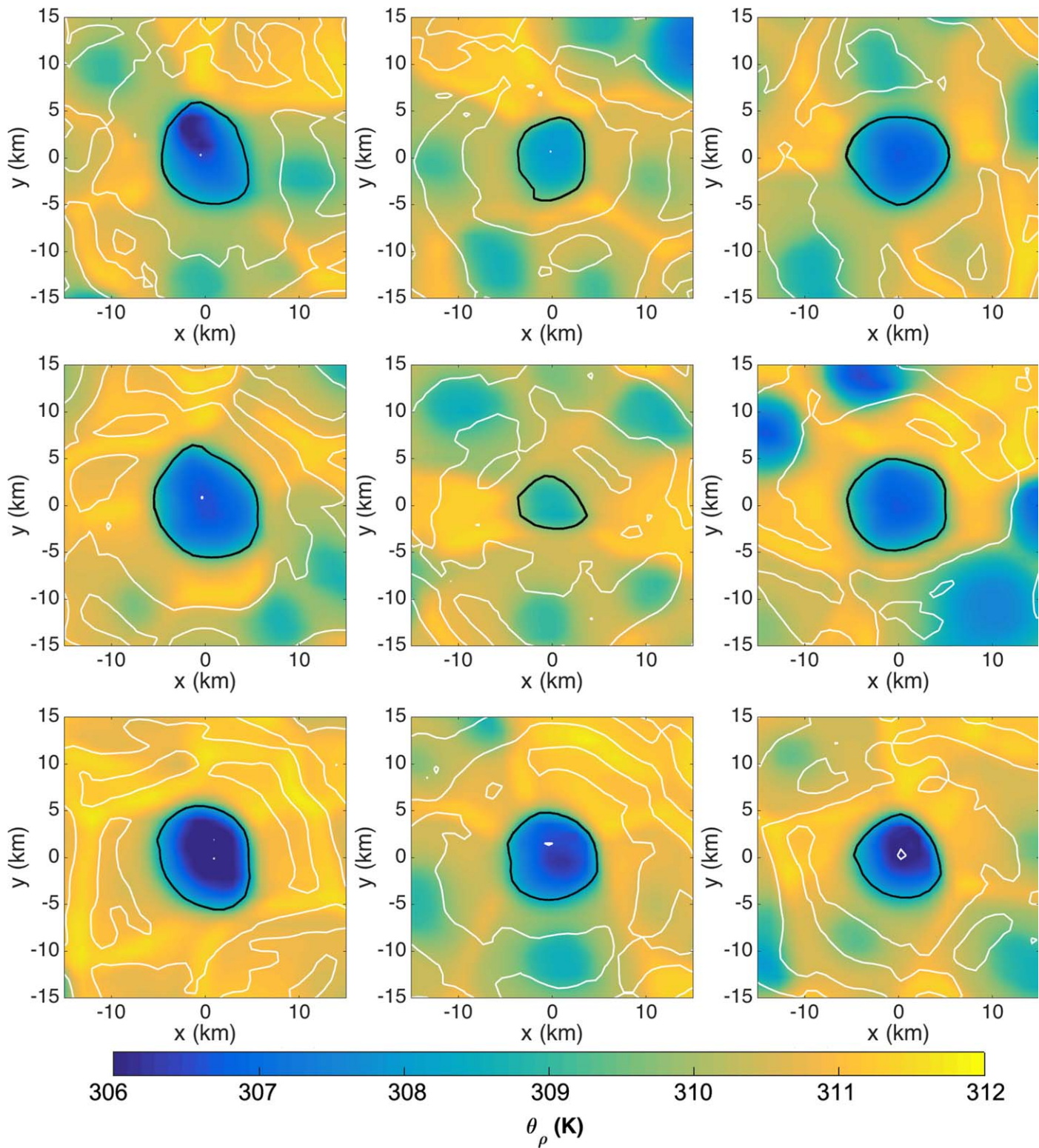


**Figure 10.** Algorithm performance for nine sample cold pools. The  $\theta_\rho$  field is plotted in colors, and  $\frac{\partial^2 \theta_\rho}{\partial t^2} = 0$  contours are shown in white, except for the contours constituting the cold pool boundaries, which are shown in black.

using information from previous output times and is thus able to capture their increased size in the creation of composite cold pools. Thus, the new algorithm represents an improvement over these other two existing algorithms.

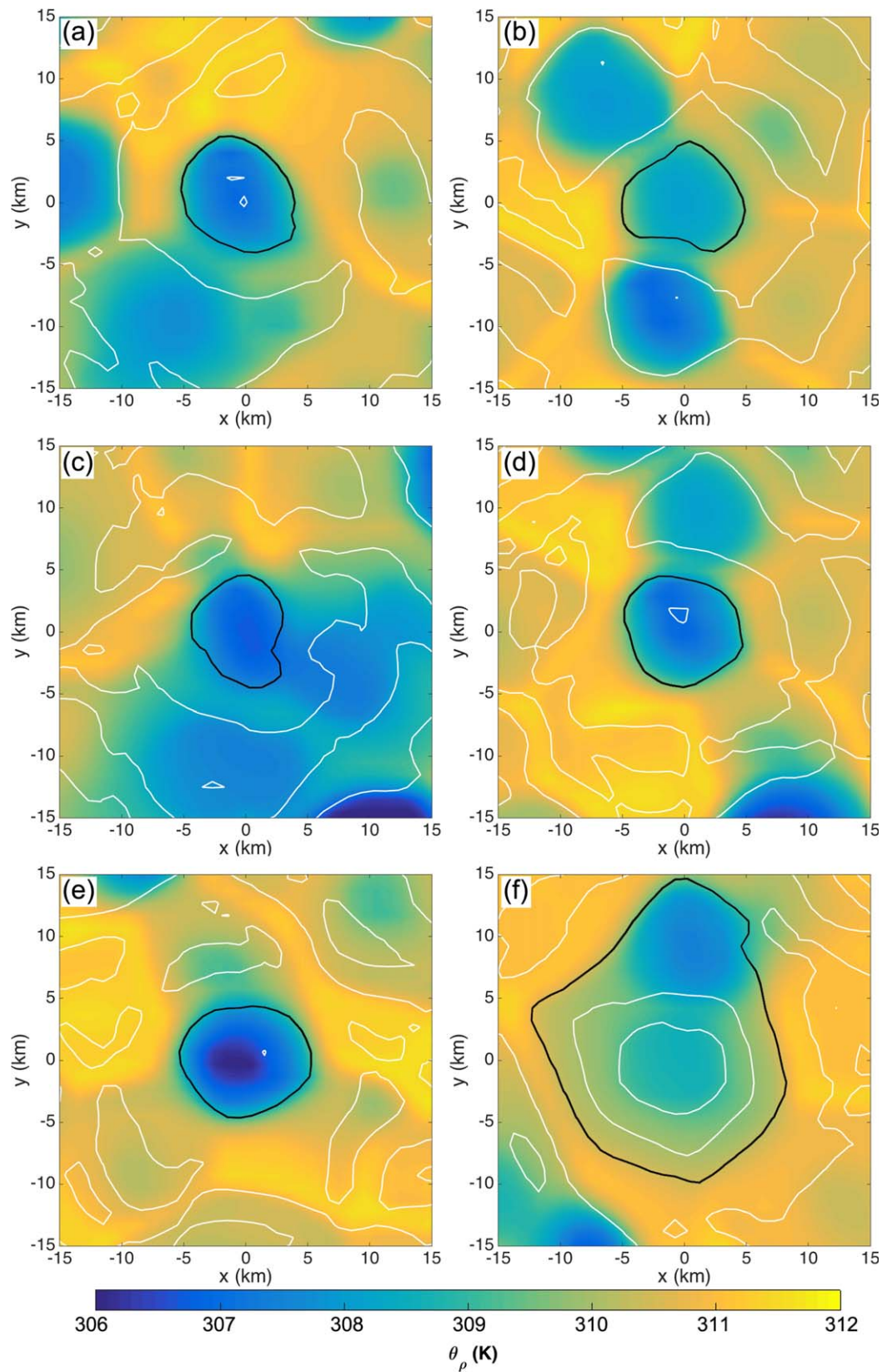


**Figure 11.** Illustration of algorithm performance for various cases. Colors and contours are as in Figure 10. Figures 11a–11d show the algorithm performance for the connected cold pool scenes shown in Figure 4. Figure 11e shows the algorithm performance for the main cold pool discussed in section 3. Figure 11f shows a case in which the algorithm does not perform well.

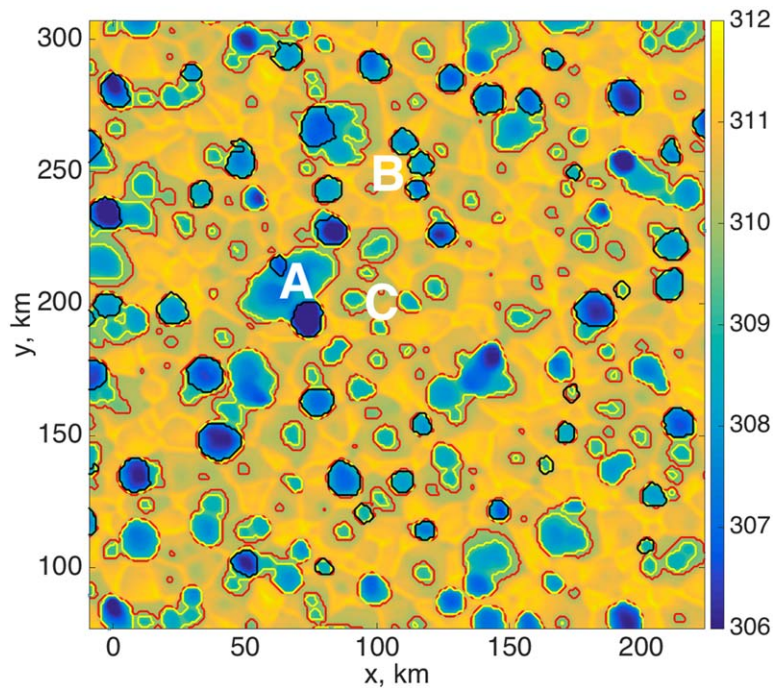


**Figure 12.** Comparison of various cold pool identification methods. Color shading is  $\theta_p$  at  $z \sim 50$  m at 14:45 LT. Black contours correspond to the cold pool boundaries obtained using the method described in this paper, i.e., using the  $\frac{\partial^2 \theta_p}{\partial r^2} = 0$  contours. Red contours correspond to the boundaries obtained using the method of Tompkins [2001] with a buoyancy threshold of  $-0.005 \text{ m s}^{-2}$ . Yellow contours correspond to the boundaries obtained using the method of Gentine *et al.* [2016]. The letters A, B, and C indicate areas of interest discussed in the text.

## 5. Composite Cold Pools

### 5.1. Overview

Figures 13 and 14 show composites of surface and near-surface quantities over time, from 30 min before until 120 min after each cold pool is identified, in 15 min increments. The composites were constructed using the 138 cold pools identified from 14:15 to 15:15 LT within the simulation described in section 2. These composites are plotted relative to the convective cold pool centroid ( $r=0$  km), henceforth referred to as the *center*. It should be noted that these composites capture a combination of cold pool evolution and the diurnal cycle. In order to help distinguish between the effects of cold pool evolution and those of the diurnal cycle, the composites are plotted out to a radius of  $r=30$  km, far enough away from the center that only the effects of the diurnal cycle should be present at this distance. It is therefore possible, by inspection, to isolate the changes in the curves due to cold pool evolution from changes due to the diurnal cycle. It should also be noted that there is some contamination from the sea breeze within these composites. Although all identified cold pools form ahead of the sea breeze, some are overtaken by the sea breeze during the two subsequent hours for which they are included in the composite cold pool calculation.

Figures 13a and 13b show the evolution of the  $\theta_p$  and  $r_v$  fields, respectively. At  $t = -30$  min,  $\theta_p$  and  $r_v$  are both elevated near the center of the future cold pool. At this time, the cold pool has not yet formed, and the elevated values of  $\theta_p$  and  $r_v$  indicate that convection preferentially develops near warm, moist perturbations within the domain. As the composite cold pool evolves, a  $\theta_p$  depression appears, peaking in strength around  $t = 0$  min, the time at which the cold pools in the composite are identified. The magnitude of the depression at this time is approximately 2.5 K. The original elevated values of  $\theta_p$  do not disappear entirely. Instead, they appear to be advected outward, forming a weak ring-like structure (i.e., a local maximum at some given radial coordinate) of enhanced  $\theta_p$  values. The  $\theta_p$  depression expands in radius as the composite cold pool grows in size, and as time progresses, the strength of the depression decreases. By  $t = 120$  min, which corresponds to 16:15 to 17:15 LT for the cold pools in the composite, the composite cold pool has dissipated, and the values of  $\theta_p$  near the cold pool center are similar to those away from the cold pool center.

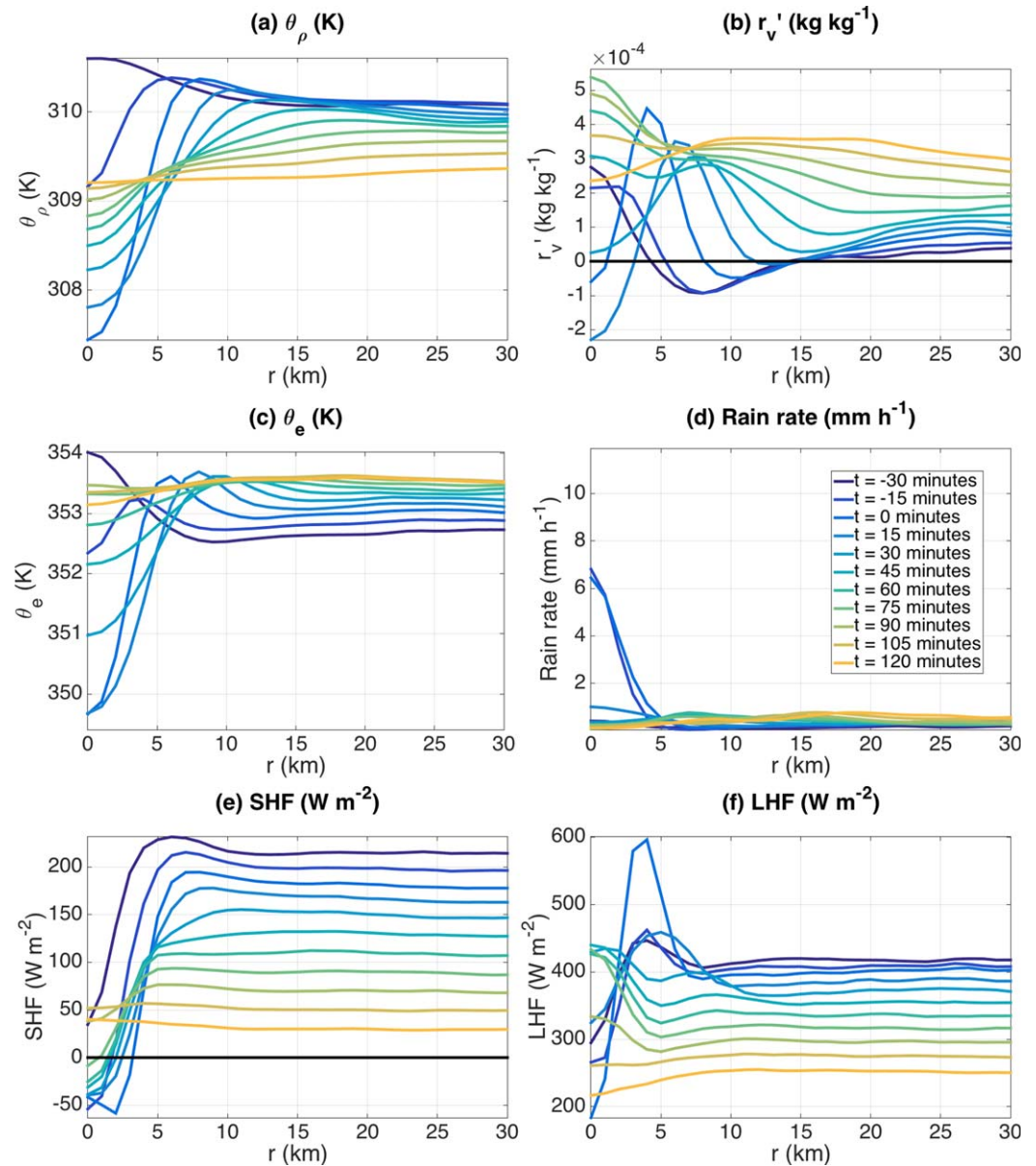


**Figure 13.** Time evolution of various composite thermodynamic and moisture variables: (a) density potential temperature  $\theta_\rho$  at  $z \sim 50$  m, (b) water vapor mixing ratio  $r_v$  at  $z \sim 50$  m, (c) equivalent potential temperature  $\theta_e$  at  $z \sim 50$  m, (d) surface rainfall rate, (e) surface sensible heat flux, and (f) surface latent heat flux.

In the  $r_v$  field, interesting trends emerge. Initially, from approximately  $t = -30$  min to  $t = -15$  min, the moist perturbation near the center expands. This expansion is likely due to the evaporation of precipitation (Figure 13d). Subsequently, a moisture ring appears: there are low values of  $r_v$  closest to the cold pool center, surrounded by significantly enhanced values of  $r_v$  around the periphery of the cold pool. The low values of  $r_v$  near the center are the result of strong, penetrating downdrafts transporting dry air from aloft.

A ring-like structure also appears in the  $\theta_e$  field, shown in Figure 13c. In agreement with the  $\theta_\rho$  and  $r_v$  composites, there are enhanced values of  $\theta_e$  at the center at  $t = -30$  min. Then, a  $\theta_e$  depression emerges in the center, and a ring of enhanced  $\theta_e$  propagates outward. The maximum magnitude of the  $\theta_e$  depression is approximately 4 K.

The cold pool also affects the surface sensible and latent heat flux fields, shown in Figures 13e and 13f, respectively. Initially, from approximately  $t = -30$  min through  $t = 15$  min, both the sensible and latent

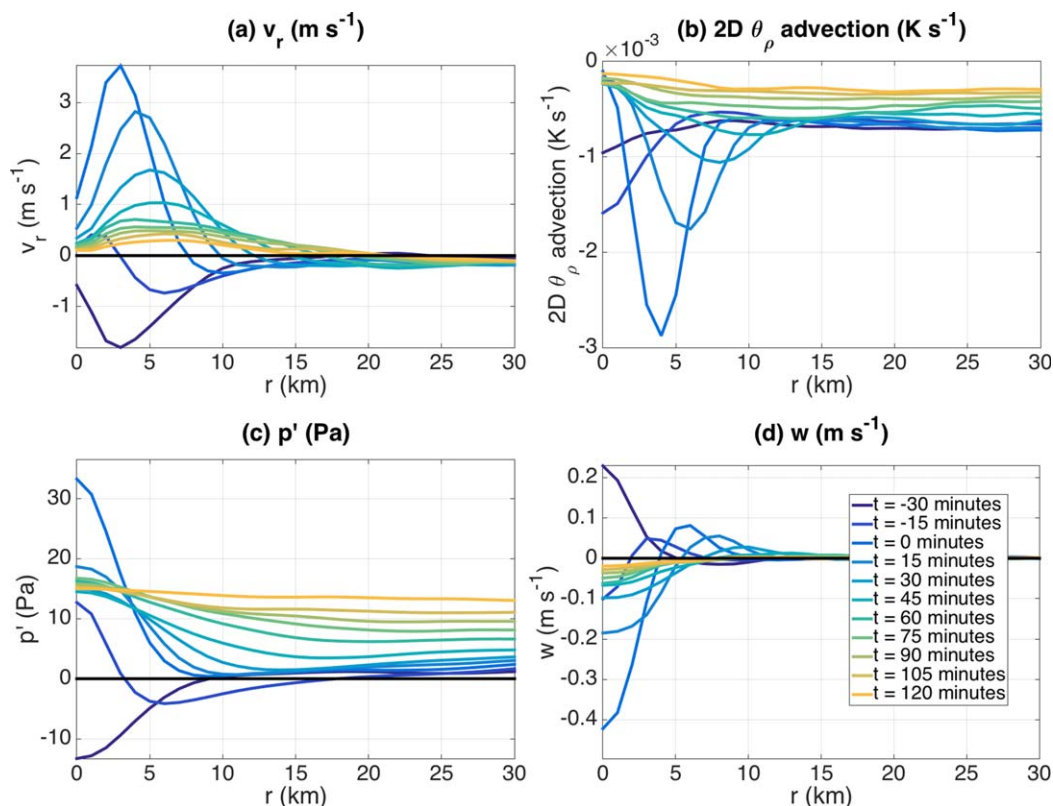


**Figure 14.** Time evolution of various composite dynamic variables: (a) radial wind  $v_r$  at  $z \sim 50$  m, (b) horizontal  $\theta_\rho$  advection at  $z \sim 50$  m, (c) perturbation pressure  $p'$  at  $z \sim 50$  m, and (d) vertical velocity  $w$  at  $z = 100$  m.

heat fluxes are suppressed near the center. This is due to shading from the cold pool's parent cloud; the reduced downwelling shortwave radiation translates into a lack of energy available to power the surface fluxes. Simultaneously, a ring-like structure appears in the latent heat flux composite, as well as, to a lesser extent, in the sensible heat flux composite. This is the wind-induced enhancement of surface heat fluxes associated with the radial winds (Figure 14a). Away from the cold pool, both the sensible and latent heat fluxes decrease with time as the evening phase of the diurnal cycle approaches.

Figure 14a shows the evolution of the radial wind field. At  $t = -30$  min, before the formation of the cold pool, there is radial inflow associated with the cold pool's parent cloud. By  $t = 0$  min this has transitioned to radial outflow associated with the developing cold pool. The location of the peak radial wind moves outward over time as the cold pool expands. The expansion of the cold pool can also be seen in the horizontal  $\theta_\rho$  advection field in Figure 14b. The magnitude of the negative  $\theta_\rho$  advection decreases with time, as does the strength of the radial outflow. These trends may be due to cold pool weakening associated with surface fluxes [e.g., Gentine et al., 2016; Grant and van den Heever, 2016]. Figure 14c shows the evolution of the pressure perturbation. At  $t = -30$  min, before the cold pool forms, there is a negative pressure perturbation. This is a hydrostatic low caused by the buoyant air aloft associated with the cold pool's parent cloud. Once the cold pool forms, the low-pressure perturbation is replaced by a high-pressure perturbation caused by a combination of hydrostatic and nonhydrostatic effects. There is nonhydrostatic high pressure near the center of the cold pool associated with the collision of downdraft air with the surface. There is also hydrostatic high pressure associated with the cool, dense cold pool air. The high-pressure perturbation persists, slowly decaying over the remainder of the cold pool lifecycle. Figure 14d shows the evolution of the vertical motion. Before the formation of the cold pool, there are near-surface updrafts, consistent with inflow associated with the cold pool's parent cloud. Updrafts soon give way to downdrafts near cold pool center surrounded by updrafts away from the center of the cold pool that occur in association with the outward propagating gust front. These results are consistent with the results presented in section 3.

### 5.2. Wet Patch

One feature that appears in several of the fields is what we will term a *wet patch*. It should be noted that this phenomenon is different from the *moist patches* of Schlemmer and Hohenegger [2014, 2016] and Torri and Kuang [2016b]. The wet patch, as defined here, is a region in which the ground has been soaked by precipitation and which has greater thermal inertia as a result. As time progresses, evaporation of the fallen precipitation on the Earth's surface through the absorption of latent heat from the ground keeps the surface cool. The cooler surface, in turn, cools the air above it via the flux of sensible heat from the atmosphere to the surface (defined in this atmospheric model framework as a negative sensible heat flux; positive sensible heat fluxes here refer to the flux of sensible heat from the surface to the atmosphere). The wet patch is visible in Figure 13e as a region of negative sensible heat fluxes. It is also visible in Figure 13f as a region of enhanced latent heat fluxes. The negative sensible heat fluxes cool the air in contact with the surface, leading to a pocket within the cold pool of especially low  $\theta_p$ , which is visible within the innermost 5 km (Figure 13a). The enhanced latent heat fluxes moisten the air sufficiently to create a region of enhanced  $r_v$ , and indeed, there is a progression over time from a ring-like structure, in which  $r_v$  is maximized at some outer radius, to a structure in which  $r_v$  is maximized near the center of the cold pool (Figure 13b). The wet patches

are difficult to discern in the  $\theta_e$  field: outside of the wet patch, insolation acts primarily to warm the air, whereas inside the wet patch, insolation acts primarily to moisten the air. Since the insolation is the same inside and outside of the wet patch, and since the calculation of  $\theta_e$  includes the effects of both warming and moistening, the  $\theta_e$  evolution is the same both inside and outside of the wet patch.

The role of the wet patch therefore appears to be to delay the recovery of the cold pool to background environmental temperatures, particularly within the center of the cold pool. The result is that new convection is especially suppressed in this region. In the early stages of cold pool growth, the wet patch has a secondary role. The soaking of the ground changes the sign of the surface sensible heat fluxes, and so when the gust front passes over the wet patch, the wind induces especially strong *negative* surface sensible heat fluxes rather than especially strong *positive* surface sensible heat fluxes. As a result, the sensible heat fluxes serve to strengthen the cold pool rather than weaken it within this region. This effect can be seen in the asymmetry of the  $v_r$  field in Figure 3c, which corresponds to the surface sensible heat flux field in Figure 7c.

It should be noted that in numerical simulations, the wet patch may exist only when it is possible for the ground to be soaked and for the surface fluxes

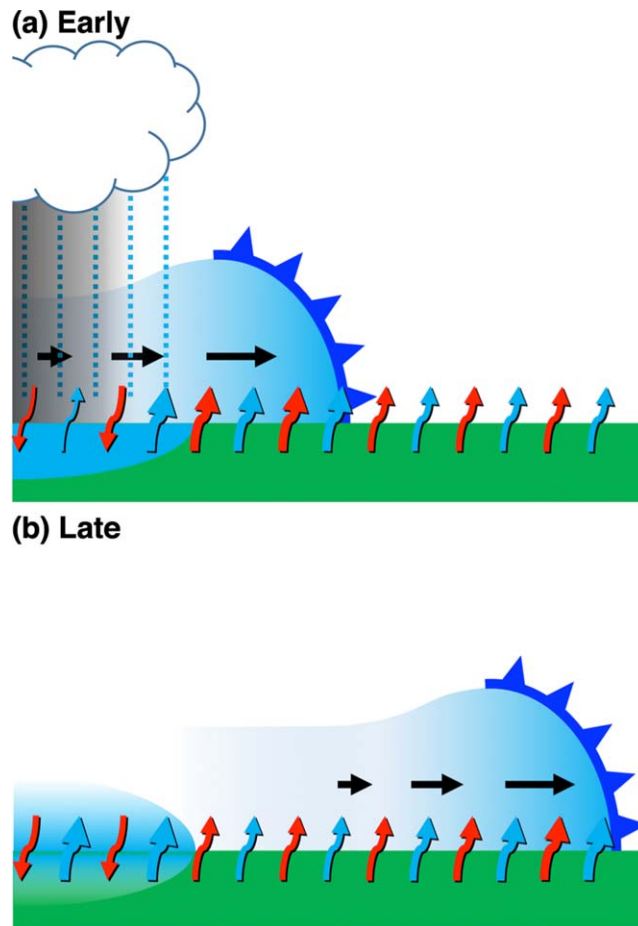


**Figure 15.** Schematic cross section of the (a) early and (b) late stages of wet patch development. The cold pool center is at left, and the green box represents the ground. The dark gray shading in Figure 15a is the cloud's shadow, which suppresses surface fluxes immediately below-cloud. Blue shading indicates excess water vapor (above ground) and soil moisture content (below ground level) relative to the mean. Black, blue, and red arrows indicate horizontal surface winds (i.e., the gust front), surface latent heat fluxes, and surface sensible heat fluxes, respectively. The red arrows directed into the ground indicate negative sensible heat fluxes within the wet patch.

to respond. This is the value of using a model like RAMS that includes a coupled, interactive land surface scheme.

## 6. Summary and Conclusions

In this paper, we have set out to develop a new approach to identifying tropical convective cold pools in numerical simulations. First, cold pool structure is investigated in terms of a variety of different state variables based on simulated cold pools. This investigation highlights features, such as sharp gradients in density potential temperature, that define cold pool edges. Based on this analysis, we then develop a novel approach to identifying and tracking convective cold pools in numerical model simulations. This approach differs from previous approaches in that it is able both to differentiate between connected convective cold pools and to determine cold pool edges without the use of an arbitrary buoyancy or other threshold (with the exception of initial rainfall rates used to obtain the basic region of cold pool development). The cold pool identification and tracking algorithm is applied to a numerical simulation of tropical convection, and a composite cold pool is generated and analyzed.

The results of both the initial and composite analyses generally agree with previous studies showing lowered temperatures, rings of enhanced water vapor, and enhanced radial winds. One novel result, made possible by the use of an interactive land surface model, is the appearance of a wet patch in the later stages of the cold pool lifecycle. The wet patch is formed by the evaporation of rainwater off a surface that has been soaked by precipitation during the initial stages of the cold pool lifecycle. The characteristics of the wet patch are as follows: (i) negative sensible heat fluxes, (ii) enhanced latent heat fluxes, (iii) cool temperatures, (iv) enhanced water vapor, and (v) enhanced sinking motion. Figure 15 summarizes these qualities in a schematic. The negative sensible heat fluxes prevent the recovery of temperature to that of the background environment within the wet patches, thus helping to extend the lifetime of the cold pool. This has implications for convective organization in that convection in the wet patch region is suppressed for a longer period of time than it would be if there were no wet patch. The negative sensible heat fluxes also act to strengthen the cold pool and thus its outward propagation, thereby increasing the likelihood of convective initiation.

The cold pool identification algorithm is based on two variables: the surface rainfall rate and the density potential temperature. Both of these variables relate to physical processes in the cold pool. Precipitation is necessary in order to initiate a convective cold pool; without precipitation there is no melting or evaporative cooling, and without significant surface rainfall, penetrating downdrafts are unlikely [Barnes and Garstang, 1982]. Cold pool edges are density currents [e.g., Charba, 1974], and thus the density potential temperature is directly related to cold pool propagation speed. The algorithm uses the rainfall field in order to identify regions in which a cold pool is likely to form, and the algorithm uses the density potential temperature field to identify cold pool edges. The latter task is accomplished using the zero contour of the second radial derivative of density potential temperature, and thus the difficult task of determining a buoyancy threshold for defining cold pool edges is avoided.

The cold pool identification algorithm is not without limitations. The algorithm requires the specification of a somewhat arbitrary rainfall rate cutoff, and it does not attempt to quantify cold pool depth. One limitation of the compositing method is that it assumes that cold pools are approximately stationary and approximately circular or elliptical. It is difficult to anticipate how well the algorithm will perform in environments with greater shear or with more widespread precipitation as might occur in the midlatitudes. Another limitation of the compositing method is that it does not normalize according to cold pool size prior to azimuthal averaging across a single cold pool or compositing across multiple cold pools. Therefore, there is some “blurring” of various features in the composite cold pools as discussed in Langhans and Romps [2015]. Furthermore, as with any numerical modeling endeavor, the validity of any results obtained using the cold pool identification algorithm is limited by the ability of the model to simulate the cold pools in question. Notably, the simulation analyzed here uses grid spacing of 1 km in the horizontal and  $\sim 100$  m (near surface) in the vertical, whereas Grant and van den Heever [2016] recommend that process studies of cold pools use grid spacings no coarser than 100 m in the horizontal and 50 m in the vertical. Therefore, we can expect that the representation of some cold pool processes and structures, such as in the surface fluxes and turbulent fluctuations, will not be resolved. However, many simulations of cold

pool-generating storms are still conducted at similar or even much coarser resolutions compared to those used here, and it is therefore still valuable to be able to track cold pools in such simulations. While the details of the algorithm may need modification in order to analyze cold pools at large-eddy simulation-type resolution, the key scientific finding presented here, i.e., the identification of the wet patch, should not be highly resolution-dependent. Caveats aside, the algorithm does a remarkable job identifying cold pool edges, and it can be used to generate useful statistics about cold pool evolution. Comparison between this algorithm and two other cold pool identification algorithms reveals that that this new algorithm is less likely to interpret clusters of cold pools as single cold pools or to mischaracterize larger, older cold pools as small ones. Importantly, this algorithm also provides a framework in which average cold pool properties can be compared from one simulation to the next. For example, efforts are currently underway to compare the cold pools examined here with ensembles of simulated cold pools in which the initial soil moisture is varied.

### Acknowledgments

The authors would like to acknowledge Leah Grant for providing the simulation data analyzed in this study. The authors would also like to thank three anonymous reviewers for their thoughtful comments that helped to improve the manuscript and Pierre Gentine for sharing the code to implement his algorithm. This work was supported by a graduate fellowship from the American Meteorological Society; the National Science Foundation Graduate Research Fellowship Program under grant DGE-1321845 Amend 5; and the U.S. Department of Energy, Office of Science, Office of Biological and Environmental Research under award DE-SC0010569. The data supporting this paper's conclusions may be obtained from Aryeh J. Drager at Aryeh.Drager@colostate.edu.

### References

- Addis, R. P., M. Garstang, and G. D. Emmitt (1984), Downdrafts from tropical oceanic cumuli, *Boundary Layer Meteorol.*, *28*(1), 23–49, doi:10.1007/BF00119455.
- Barnes, G. M., and M. Garstang (1982), Subcloud layer energetics of precipitating convection, *Mon. Weather Rev.*, *110*(2), 102–117, doi:10.1175/1520-0493(1982)110<0102:SLEOPC>2.0.CO;2.
- Charba, J. (1974), Application of gravity current model to analysis of squall-line gust front, *Mon. Weather Rev.*, *102*(2), 140–156, doi:10.1175/1520-0493(1974)102<0140:AOGCMT>2.0.CO;2.
- Cotton, W. R., et al. (2003), RAMS 2001: Current status and future directions, *Meteorol. Atmos. Phys.*, *82*(1), 5–29, doi:10.1007/s00703-001-0584-9.
- Dawson, D. T., M. Xue, J. A. Milbrandt, and M. K. Yau (2010), Comparison of evaporation and cold pool development between single-moment and multimoment bulk microphysics schemes in idealized simulations of tornadic thunderstorms, *Mon. Weather Rev.*, *138*(4), 1152–1171, doi:10.1175/2009MWR2956.1.
- DeMott, P. J., A. J. Prenni, X. Liu, S. M. Kreidenweis, M. D. Petters, C. H. Twohy, M. S. Richardson, T. Eidhammer, and D. C. Rogers (2010), Predicting global atmospheric ice nuclei distributions and their impacts on climate, *Proc. Natl. Acad. Sci. U. S. A.*, *107*(25), 11,217–11,222, doi:10.1073/pnas.0910818107.
- Doswell, C. A., and P. M. Markowski (2004), Is buoyancy a relative quantity?, *Mon. Weather Rev.*, *132*(4), 853–863, doi:10.1175/1520-0493(2004)132<0853:IBARO>2.0.CO;2.
- Droegemeier, K. K., and R. B. Wilhelmson (1985), Three-dimensional numerical modeling of convection produced by interacting thunderstorm outflows. Part I: Control simulation and low-level moisture variations, *J. Atmos. Sci.*, *42*(22), 2381–2403, doi:10.1175/1520-0469(1985)042<2381:TDNMO>2.0.CO;2.
- Emanuel, K. A. (1994), *Atmospheric Convection*, Oxford Univ. Press, New York.
- Engerer, N. A., D. J. Stensrud, and M. C. Coniglio (2008), Surface characteristics of observed cold pools, *Mon. Weather Rev.*, *136*(12), 4839–4849, doi:10.1175/2008MWR2528.1.
- Feng, Z., S. Hagos, A. K. Rowe, C. D. Burleyson, M. N. Martini, and S. P. de Szoeke (2015), Mechanisms of convective cloud organization by cold pools over tropical warm ocean during the AMIE/DYNAMO field campaign, *J. Adv. Model. Earth Syst.*, *7*, 357–381, doi:10.1002/2014MS000384.
- Fisher, R. B., T. P. Breckon, K. Dawson-Howe, A. Fitzgibbon, C. Robertson, E. Trucco, and C. K. I. Williams (2014), *Dictionary of Computer Vision and Image Processing*, 2nd ed., John Wiley, Chichester, West Sussex, U. K.
- Gentine, P., A. Garelli, S. B. Park, J. Nie, G. Torri, and Z. Kuang (2016), Role of surface heat fluxes underneath cold pools, *Geophys. Res. Lett.*, *43*, 874–883, doi:10.1002/2015GL067262.
- Goff, R. C. (1976), Vertical structure of thunderstorm outflows, *Mon. Weather Rev.*, *104*(11), 1429–1440, doi:10.1175/1520-0493(1976)104<1429:VSOTO>2.0.CO;2.
- Grant, L. D., and S. C. van den Heever (2014), Aerosol-cloud-land surface interactions within tropical sea breeze convection, *J. Geophys. Res. Atmos.*, *119*, 8340–8361, doi:10.1002/2014JD021912.
- Grant, L. D., and S. C. van den Heever (2015), Cold pool and precipitation responses to aerosol loading: Modulation by dry layers, *J. Atmos. Sci.*, *72*(4), 1398–1408, doi:10.1175/JAS-D-14-0260.1.
- Grant, L. D., and S. C. van den Heever (2016), Cold pool dissipation, *J. Geophys. Res. Atmos.*, *121*, 1138–1155, doi:10.1002/2015JD023813.
- Harrington, J. Y. (1997), The effects of radiative and microphysical processes on simulated warm and transition season Arctic stratus, PhD thesis, Colo. State Univ., Fort Collins.
- Hill, G. E. (1974), Factors controlling the size and spacing of cumulus clouds as revealed by numerical experiments, *J. Atmos. Sci.*, *31*(3), 646–673, doi:10.1175/1520-0469(1974)031<0646:FCTSAS>2.0.CO;2.
- Jeevanjee, N., and D. M. Romps (2013), Convective self-aggregation, cold pools, and domain size, *Geophys. Res. Lett.*, *40*, 994–998, doi:10.1002/grl.50204.
- Katona, B. T., A. McGovern, V. Lakshmanan, and A. J. Clark (2014), Automated identification of cold pools in a convection-permitting model, in *12th Conference on Artificial and Computational Intelligence and its Applications to the Environmental Sciences*, American Meteorological Society, Atlanta, Ga.
- Khairoutdinov, M., and D. Randall (2006), High-resolution simulation of shallow-to-deep convection transition over land, *J. Atmos. Sci.*, *63*(12), 3421–3436, doi:10.1175/JAS3810.1.
- Kilpatrick, T. J., and S.-P. Xie (2015), ASCAT observations of downdrafts from mesoscale convective systems, *Geophys. Res. Lett.*, *42*, 1951–1958, doi:10.1002/2015GL063025.
- Klemp, J. B., and R. B. Wilhelmson (1978), The simulation of three-dimensional convective storm dynamics, *J. Atmos. Sci.*, *35*(6), 1070–1096, doi:10.1175/1520-0469(1978)035<1070:TSOTDC>2.0.CO;2.
- Langhans, W., and D. M. Romps (2015), The origin of water vapor rings in tropical oceanic cold pools, *Geophys. Res. Lett.*, *42*, 7825–7834, doi:10.1002/2015GL065623.

- Li, Z., P. Zuidema, and P. Zhu (2014), Simulated convective invigoration processes at trade wind cumulus cold pool boundaries, *J. Atmos. Sci.*, *71*, 2823–2841, doi:10.1175/JAS-D-13-0184.1.
- Lilly, D. K. (1962), On the numerical simulation of buoyant convection, *Tellus*, *14*(2), 148–172, doi:10.1111/j.2153-3490.1962.tb00128.x.
- Meyers, M. P., R. L. Walko, J. Y. Harrington, and W. R. Cotton (1997), New RAMS cloud microphysics parameterization. Part II: The two-moment scheme, *Atmos. Res.*, *45*(1), 3–39, doi:10.1016/S0169-8095(97)00018-5.
- Redl, R., A. H. Fink, and P. Knippertz (2015), An objective detection method for convective cold pool events and its application to Northern Africa, *Mon. Weather Rev.*, *143*(12), 5055–5072, doi:10.1175/MWR-D-15-0223.1.
- Rotunno, R., J. B. Klemp, and M. L. Weisman (1988), A theory for strong, long-lived squall lines, *J. Atmos. Sci.*, *45*(3), 463–485, doi:10.1175/1520-0469(1988)045<0463:ATFSL>2.0.CO;2.
- Saleeby, S. M., and W. R. Cotton (2004), A large-droplet mode and prognostic number concentration of cloud droplets in the Colorado State University regional atmospheric modeling system (RAMS). Part I: Module descriptions and supercell test simulations, *J. Appl. Meteorol.*, *43*(1), 182–195, doi:10.1175/1520-0450(2004)043<0182:ALMAPN>2.0.CO;2.
- Saleeby, S. M., and S. C. van den Heever (2013), Developments in the CSU-RAMS aerosol model: Emissions, nucleation, regeneration, deposition, and radiation, *J. Appl. Meteorol. Climatol.*, *52*(12), 2601–2622, doi:10.1175/JAMC-D-12-0312.1.
- Schlemmer, L., and C. Hohenegger (2014), The formation of wider and deeper clouds as a result of cold-pool dynamics, *J. Atmos. Sci.*, *71*(8), 2842–2858, doi:10.1175/JAS-D-13-0170.1.
- Schlemmer, L., and C. Hohenegger (2016), Modifications of the atmospheric moisture field as a result of cold-pool dynamics, *Q. J. R. Meteorol. Soc.*, *142*(694), 30–42, doi:10.1002/qj.2625.
- Seigel, R. B. (2014), Shallow cumulus mixing and subcloud-layer responses to variations in aerosol loading, *J. Atmos. Sci.*, *71*(7), 2581–2603, doi:10.1175/JAS-D-13-0352.1.
- Simpson, J. E. (1969), A comparison between laboratory and atmospheric density currents, *Q. J. R. Meteorol. Soc.*, *95*(406), 758–765, doi:10.1002/qj.49709540609.
- Smagorinsky, J. (1963), General circulation experiments with the primitive equations I. The basic experiment, *Mon. Weather Rev.*, *91*(3), 99–164, doi:10.1175/1520-0493(1963)091<0099:GCEWTP>2.3.CO;2.
- Terai, C. R., and R. Wood (2013), Aircraft observations of cold pools under marine stratocumulus, *Atmos. Chem. Phys.*, *13*(19), 9899–9914, doi:10.5194/acp-13-9899-2013.
- Tompkins, A. M. (2001), Organization of tropical convection in low vertical wind shears: The role of cold pools, *J. Atmos. Sci.*, *58*(13), 1650–1672, doi:10.1175/1520-0469(2001)058<1650:OOTCIL>2.0.CO;2.
- Torri, G., and Z. Kuang (2016a), A Lagrangian study of precipitation-driven downdrafts, *J. Atmos. Sci.*, *73*(2), 839–854, doi:10.1175/JAS-D-15-0222.1.
- Torri, G., and Z. Kuang (2016b), Rain evaporation and moist patches in tropical boundary layers, *Geophys. Res. Lett.*, *43*, 9895–9902, doi:10.1002/2016GL070893.
- Torri, G., Z. Kuang, and Y. Tian (2015), Mechanisms for convection triggering by cold pools, *Geophys. Res. Lett.*, *42*, 1943–1950, doi:10.1002/2015GL063227.
- Uyeda, H., and D. S. Zrnić (1986), Automatic detection of gust fronts, *J. Atmos. Oceanic Technol.*, *3*(1), 36–50, doi:10.1175/1520-0426(1986)003<0036:ADOGF>2.0.CO;2.
- Walko, R. L., et al. (2000), Coupled atmosphere–biophysics–hydrology models for environmental modeling, *J. Appl. Meteorol.*, *39*(6), 931–944, doi:10.1175/1520-0450(2000)039<0931:CABHMF>2.0.CO;2.
- Warner, C., J. Simpson, G. Van Helvoirt, D. W. Martin, D. Suchman, and G. L. Austin (1980), Deep convection on day 261 of GATE, *Mon. Weather Rev.*, *108*(2), 169–194, doi:10.1175/1520-0493(1980)108<0169:DCODOG>2.0.CO;2.
- Weisman, M. L., and R. Rotunno (2004), “A theory for strong, long-lived squall lines” revisited, *J. Atmos. Sci.*, *61*(4), 361–382, doi:10.1175/1520-0469(2004)061<0361:ATFSL>2.0.CO;2.
- Wilbanks, M. C., S. E. Yuter, S. P. de Szoeke, W. A. Brewer, M. A. Miller, A. M. Hall, and C. D. Burleyson (2015), Near-surface density currents observed in the Southeast Pacific stratocumulus-topped marine boundary layer, *Mon. Weather Rev.*, *143*(9), 3532–3555, doi:10.1175/MWR-D-14-00359.1.
- Yokoi, S., M. Katsumata, and K. Yoneyama (2014), Variability in surface meteorology and air-sea fluxes due to cumulus convective systems observed during CINDY/DYNAMO, *J. Geophys. Res. Atmos.*, *119*, 2064–2078, doi:10.1002/2013JD020621.
- Young, G. S., S. M. Perugini, and C. W. Fairall (1995), Convective wakes in the equatorial Western Pacific during TOGA, *Mon. Weather Rev.*, *123*, 110–123, doi:10.1175/1520-0493(1995)123<0110:CWITEW>2.0.CO;2.